



Remote sensing techniques and geochemical constraints on the formation of the Wadi El-Hima mineralized granites, Egypt: new insights into the genesis and accumulation of garnets

Mohamed Zaki Khedr¹ · Saif M. Abo Khashaba¹ · N. H. El-Shibiny¹ · Reda A. El-Arafy² · Eiichi Takazawa³ · Mokhles K. Azer⁴ · Richard. M. Palin⁵

Received: 29 March 2022 / Accepted: 25 July 2022 / Published online: 20 August 2022
© The Author(s) 2022

Abstract

The Wadi El-Hima Neoproterozoic I- and A-type granites in the Southern Eastern Desert of Egypt are rich in garnets (up to 30 vol%) and are cut by NW–SE strike-slip faults, as confirmed from structure lineament extraction maps. These mineralized granites and garnet mineralization zones can be successfully discriminated using remote sensing techniques. Spectral angle mapper and matched filtering techniques are highly effective for mapping garnet-rich zones and show that the highest garnet concentrations occur along the intrusive contact zone of NW–SE striking faults. El-Hima granites have high SiO₂ (73.5–75.1 wt%), Al₂O₃ (13.4–15.3 wt%) and total alkali (6.7–8.7 wt%) contents, suggesting that they were sourced from peraluminous (A/CNK > 1) parental magmas. Garnet-bearing trondhjemites are metasomatic in origin and formed after I-type tonalite-granodiorites, which originated in a volcanic arc tectonic setting. Garnet-rich syenogranites and alkali-feldspar granites are both post-collisional A-type granites: the syenogranites formed from peraluminous magmas generated by partial melting of lower crustal tonalite and metasedimentary protoliths during lithospheric delamination, and the alkali-feldspar granites crystallized from highly fractionated, felsic and alkali-rich peraluminous magmas in the upper crust. Garnets in El-Hima mineralized granites occur in three forms: (1) subhedral disseminated crystals, (2) vein-type crystals, and (3) aggregated subhedral crystals, reflecting different mechanisms of accumulation. All are dominantly almandine in composition (Alm₇₆Sps₁₀Prp₇Grs₆Adr₁) and have high average concentrations of heavy rare earth elements (HREE) (ΣHREE = 1636 ppm), Y (3394 ppm), Zn (325 ppm), Li (39.17 ppm) and Ga (34.94 ppm). Garnet REE patterns show strong negative Eu anomalies with HREE enriched relative to LREE, indicating a magmatic origin. These magmatic garnets are late-stage crystallization products of Al-rich hydrous magmas, and formed at low temperature (680–730 °C) and pressure (2.1–2.93 kbar) conditions in the upper continental crust. Peculiar garnet concentrations in syenogranites near and along contact zones with alkali feldspar granites are related to peraluminous parent hydrous magma compositions. These garnets formed by in situ crystallization from A-type granite melts, alongside accumulation of residual garnets left behind after partial melting of the host garnet-rich granites along the intrusive contact. Magmatic-fluid flow along the NW–SE striking fault of Najd system enhanced garnet accumulation in melts, which formed clots and veins of garnet.

Keywords Mineralized granites · Garnet genesis · Almandine-rich garnet · ASTER data · Spectral angle mapper · Matched filtering

Introduction

The Wadi El-Hima area is located in the Southern Eastern Desert of Egypt, and comprises mineralized I- and A-type granites associated with ophiolitic mélangé and gneisses. These Neoproterozoic rocks are part of the Arabian-Nubian Shield (ANS). The Neoproterozoic (950–550 Ma; Stern 2002) ANS contains voluminous granites that are mostly free of garnets, except for a small number of localities,

✉ Mohamed Zaki Khedr
mohamed.khader1@sci.kfs.edu.eg; khedrzm75@gmail.com

Extended author information available on the last page of the article

including the studied Wadi El-Hima area (Fig. 1a). Key granite plutons in the Eastern Desert of Egypt that are rich in magmatic garnets include: (1) the Wadi Sikiat I-type granites, which contain ~4 vol% of almandine (55–64 mol%)-rich garnets (Moghazi et al. 2004), and are similar in composition to Wadi El-Hima I- and A-type granites; (2) the Abu Had S-type granites (10 vol% garnet) and pegmatites (30 vol% garnet) contain almandine (32–48 mol%)- and spessartine (30–56 mol%)-rich garnets (Gharib 2012); (3) the Abu Diab A-type granites, which include up to 2 vol% garnets that are spessartine (61–72 mol%) to almandine (25–35 mol%) in composition (Sami et al. 2020). These garnets and their hosting fractionated A-type granites likely crystallized from peraluminous magmas in an anorogenic or extensional tectonic environment (du Bray 1988; Sami et al. 2020; Seddik et al. 2020).

Garnet occurs in many granitic rock types as an accessory phase, and may have a range in compositions, but requires certain petrogenetic conditions to crystallize. Some mineralized granites are unusually rich in garnet (15–40 vol%), including garnet-rich zones (30 vol% garnet) in granite from the South Mountain Batholith (Erdmann et al. 2009) and garnet aggregations (30–40 vol%) in peraluminous granitic rocks from the Flagstaff Lake igneous complex (Dorais and Campbell 2022). Up to 15 vol% garnet may form in S-type granites (Rene and Stelling 2007) derived from partial melting of metasedimentary crustal rocks (Chappell and White 1974). In contrast, I- and A-type peraluminous granites (du Bray 1988; Zhang et al. 2017) contain much less magmatic garnet (<4 vol%) than S-type granites, although the studied El-Hima I- and A-type granites contain garnet, mainly 4–10 vol%. Garnet is an important geochemical indicator due to its ability to fractionate HREE from LREE (Gaspar et al. 2008); thus, its origin and occurrence in granites have been the focus of many recent studies that have investigated the sources of granitic magmas and post-magmatic metasomatism (Gharib 2012; Samadi et al. 2014; Zhou et al. 2017; Sami et al. 2020; Seddik et al. 2020).

Magmatic garnet in igneous rocks is subdivided into three groups: (1) garnet in strongly peraluminous S-type dacites-rhyolites or granites, which crystallized at low pressures in the upper crust, and has high FeO (>30 wt%) contents (Clemens and Wall 1981, 1984; Rene and Stelling 2007), similar to low-pressure garnets in the Wadi El-Hima mineralized granites; (2) garnet in basalts, andesites, dacites, rhyolites or tonalitic and granodioritic porphyries that crystallized at high pressure in the lower crust or mantle, and which has 20–30 wt% FeO, 5–10 wt% MgO, and ~5 wt% CaO (Green and Ringwood 1968; Harangi et al. 2001); and (3) garnet in pegmatites, aplites, and granites that crystallized from post-magmatic fluids or from highly fractionated magmas, and which is strongly enriched in MnO (~30 wt%), but relatively depleted in FeO (10–15 wt%) (Speer and Becker 1992).

Remote sensing satellite data, such as Advanced Spaceborne Thermal Emission and Reflection Radiometer (ASTER) imagery, can provide complementary data for rock discrimination and mineral exploration (e.g., Aboelkhair et al. 2010; Amer et al. 2010; Asran et al. 2017; Izawa et al. 2018; Shawky et al. 2019). Although silicates can be detected using Thermal Infrared (TIR), some silicate mineral groups, such as garnet, can be detected in the region of visible-near infrared (VNIR) and short wave infrared (SWIR) of ASTER satellite sensor (Izawa et al. 2018), due to a distinctive absorption characteristic in the Si–O bond that can be detected in the thermal emission region of the electromagnetic wavelength. However, TIR bands in the ASTER sensor have a smaller radiometric and spatial resolution (90 m) compared to VNIR-SWIR bands (i.e. 30 m). The spectral reflectance properties of garnets in the wavelength range (0.35–2.5 μm) suggest that garnets can be detected using ASTER sensor data in VNIR + SWIR bands based on their composition and structure (Izawa et al. 2018). In this study, spectral remote sensing mapping techniques such as automatic lineaments extraction, matched filtering (MF) and spectral angle mapper (SAM) have been used to detect garnet mineralization in host granites and stream sediments from the Wadi El-Hima area in the South Eastern Desert. Using these techniques, Wadi El-Hima mineralized granites have been discovered along intrusive contacts associated with a NW–SE striking tensional fault zone related to the Najd fault system in the Eastern Desert, similar to Abu Dabbab mineralized granites that occur along other NW–SE striking tensional fault zones (Heikal et al. 2019).

We present an integrated study involving field observations, different remote sensing spectral mapping techniques for discrimination of both rock units and garnet-rich zones, mineral chemistry (major, trace and REE) and whole-rock chemistry for Neoproterozoic mineralized granites and some stream sediments. This work aims to shed light on the timing of garnet genesis, its mode of occurrence, chemistry, and mechanisms of accumulation, as well as the factors controlling garnet mineralization in the Wadi El-Hima I- and A-type granites. This study also discusses the petrogenesis and geodynamic evolution of Wadi El-Hima granitic plutons in the context of tectonic and structural trends in the Eastern Desert of Egypt. As such, we emphasize the usefulness of remote sensing techniques for discrimination of mineralized granites and garnet mapping using ASTER satellite sensor bands of VNIR and SWIR.

Geologic setting

The Wadi El-Hima area is located ~50 km south of the Idfu-Marsa Allam road and ~80 km southwest of Marsa Allam City (Fig. 1a). The area (93 km²) is dissected by several

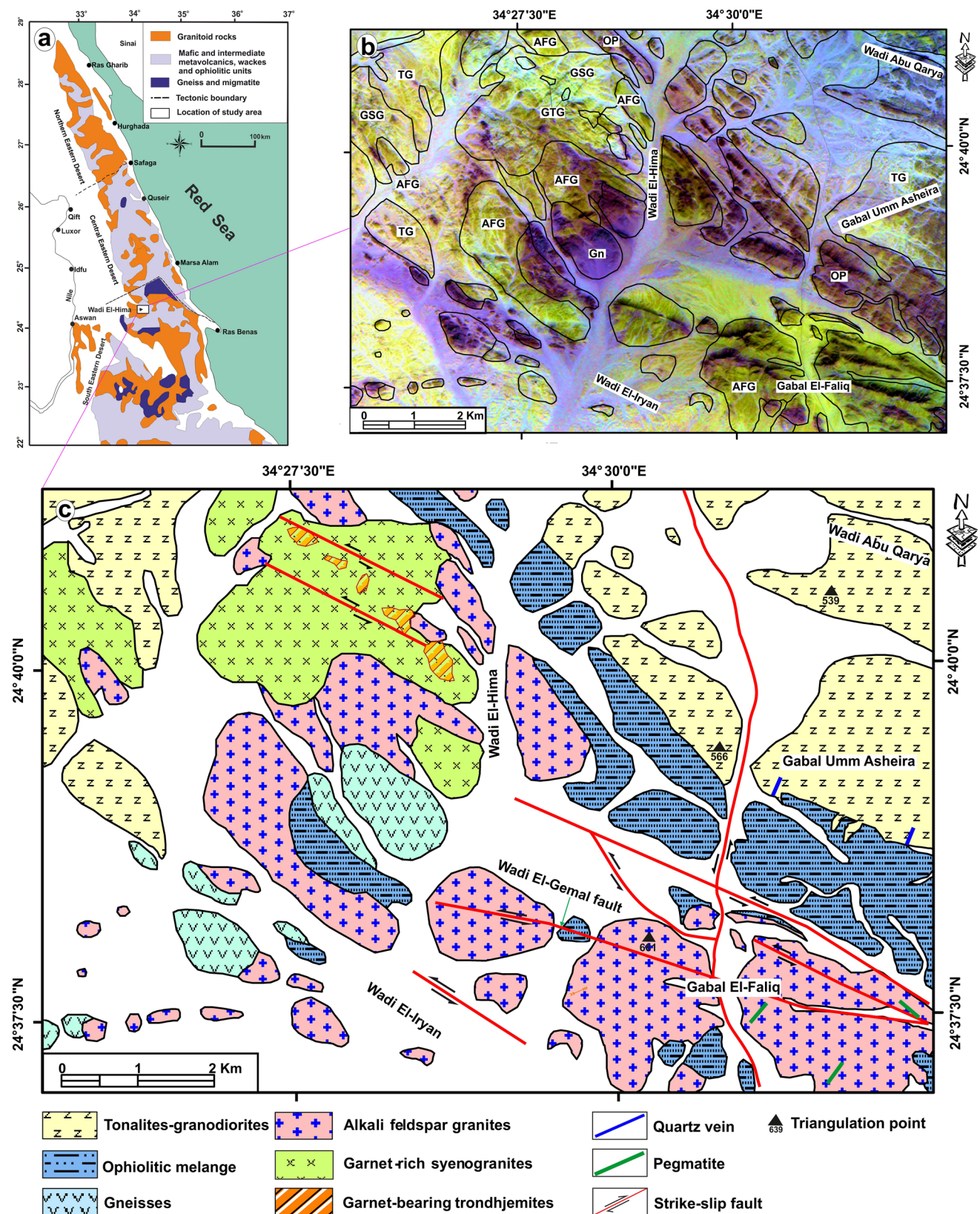


Fig. 1 Remote sensing and geological map of the Wadi El-Hima area. **a** Location map of the study area (Stern and Hedge 1985). **b** ASTER false colour composite image (RGB=981). **c** Geological map of the Wadi El-Hima area produced from integrated remote sens-

ing techniques and field study, modified from Saleh et al. (2014). Gn, gneisses; OP, ophiolitic rocks; TG, tonalites-granodiorites; GTR, garnet-bearing trondhjemites; GSG, garnet-rich syenogranites; AFG, alkali feldspar granites

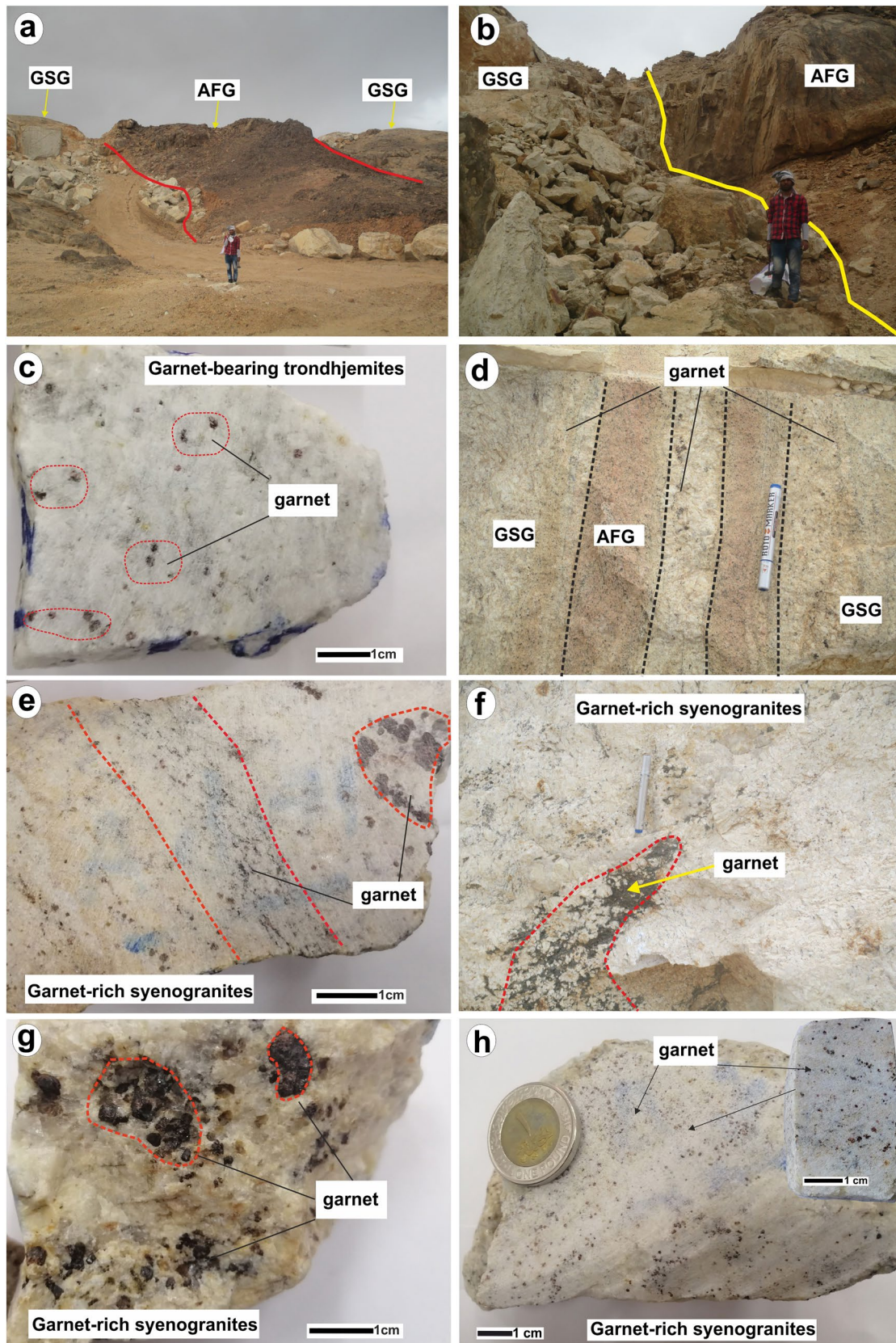


Fig. 2 Field photographs and hand specimen samples of Wadi El-Hima granites. **a** Panorama view of alkali feldspar granites and garnet-rich syenogranites with clearly intrusive contacts. **b** Close up view of the contact between garnet-rich syenogranites and alkali feldspar granites. **c** Hand specimen of disseminated garnet grains in garnet-bearing trondhjemites. **d** Close-up view of garnet-bearing syenogranites inter-veined by alkali feldspar granites, forming mixed zone and garnet arranged as veins. **e** Hand specimen of garnet-rich syenogranites showing high concentrations of fine-grained garnets arranged as veins and coarse aggregated grains or clots on the rim. **f** Close-up view of garnet-bearing syenogranites with high concentrations of garnet clots in the form of a wedge shape. **g** Garnet aggregated grains or clots in garnet-rich syenogranites. **h** Disseminated and garnet aggregates in garnet-rich syenogranites showing high concentrations (up to 30 vol%). Abbreviations as in Fig. 1

Wadis, including Wadi El-Hima (Fig. 1c). We present a new geological map of the Wadi El-Hima area (Fig. 1c) based on the combined results of remote sensing processing, and field investigation. The main structure strike in the Wadi El-Hima area is NW–SE, which relates to the Wadi El-Gemal strike-slip fault and the Najd fault system (Sultan et al. 1988; Fig. 1c). This is confirmed from the dominant NW–SE striking faults based on the structure lineaments map, whereas minor structure strikes are E–W and N–S that match other Precambrian deformation structures elsewhere in Egypt. Several rock types in the Wadi El-Hima area can be distinguished from oldest to youngest, including: gneisses, ophiolitic assemblages, tonalites–granodiorites, garnet-bearing trondhjemites, garnet-rich syenogranites, alkali feldspar granites, post granitic dykes, and quartz veins (Fig. 1c). Syenogranites and alkali feldspar granites intrude into ophiolitic rocks and tonalites–granodiorites (Figs. 1c, 2a, b), and show intrusive contacts. The ophiolitic belt (Fig. 1b, c) and scattered garnet-bearing trondhjemite pockets have a NW–SE trend, which is parallel to the Najd fault system that controls ore deposits and mineralization in the Central Eastern Desert of Egypt (Heikal et al. 2019).

Garnet-bearing trondhjemites occur in the northwestern part of the mapped area as several large elongate pockets within the garnet-rich syenogranites (Fig. 1b, c). They are very low in relief, up to ~15 m in height, but each pluton can extend 20–50 m in width and 500–800 m in length at the surface. They are medium-to-coarse grained and are white in colour (Fig. 2c) due to conversion of Ca–Na plagioclase to Na-rich plagioclase during metasomatism of the precursor tonalites. Garnet-bearing trondhjemites also exhibit a gradational contact with garnet-rich syenogranites. Garnets can be observed with the naked eye as disseminated grains within the trondhjemites (Fig. 2c; Supplementary 1a), and become more abundant toward the intrusive contact with other granites.

Garnet-rich syenogranites occur as large elongate plutons that are medium- to coarse-grained and have a whitish grey (Fig. 2f, h) to pale pink colour (Fig. 2e, g; Supplementary

1a). They intrude into tonalities and granodiorites in the northwest of the Wadi El-Hima area (Fig. 1b, c). Garnet-rich syenogranites have low to moderate relief, up to 18–25 m height, and cover an area of about ~8.77 km² (Fig. 1c). They form a sharp intrusive contact with alkali feldspar granites (Fig. 2a, b) associated with a structure strike of NW–SE (Figs. 1c, 5b). Occasionally, they show a gradational contact with garnet-bearing trondhjemites. These syenogranites are occasionally veined and intruded by alkali feldspar granites (Fig. 2d).

Alkali feldspar granites cover an area of ~15.60 km² and have elongated shapes. They exist as isolated masses along both sides of Wadi El-Hima and Wadi El-Iryan (Fig. 1c), and intrude into garnet-rich syenogranites (Fig. 2a), ophiolitic rocks and gneisses rocks in these regions (Fig. 1c). Alkali feldspar granites display slightly sharp contacts with garnet-rich syenogranites (Fig. 2a, b, d) and contain disseminated garnet grains—typically with proportions of 1–4 vol%—but become more abundant at intermixed contact zones with syenogranites (Fig. 2d). Several NW–SE and NE–SW pegmatite dykes cut alkali feldspar granites at Gabal El-Faliq (Fig. 1c).

Garnets in the investigated area occur in whole rock granitic masses in all granitic types, but with different concentrations (mainly 2–8 vol% garnet) that increase toward the intrusive contact with alkali feldspar granites. They have three modes of occurrence (Fig. 2) including: (1) disseminated small subhedral to rounded crystals (Fig. 2h), (2) small to medium crystals arranged in veins or clusters (Fig. 2d, e), and (3) patches or spot-like garnet aggregates (Fig. 2e, f, g). The vein-type (Fig. 2e) and aggregated garnets (Fig. 2f, g) in syenogranites occur in higher concentrations (up to 25 vol%) along contacts with alkali feldspar granites (Fig. 2a, b) and disseminated garnet can form up to 30 vol%; Fig. 2h). The Wadi El-Gemal NW–SE strike-slip fault cuts some parts of the garnet-bearing trondhjemites and garnet-rich syenogranites (Figs. 1c, 5a).

Petrography

Garnet-bearing trondhjemites petrographically resemble metasomatized tonalites in terms of their mineral constituents and textures. They are composed mainly of plagioclase (50–55 vol%), quartz (24–28 vol%), K-feldspar (6–12 vol%), and garnet (2–6 vol%) (Fig. 3a, b) and show myrmekitic textures (Supplementary 2a). Other minor constituents include biotite and chlorite (2–4 vol%, Fig. 3a, b). Apatite, titanite, epidote, zircon, ilmenite, magnetite and titanomagnetite are accessory minerals. Sodic-plagioclase (An_{13–18}) occurs as subhedral columnar crystals, with variable grain sizes. Coarse plagioclase tabular crystals show albite twinning, whereas other crystals show normal zonation. Some

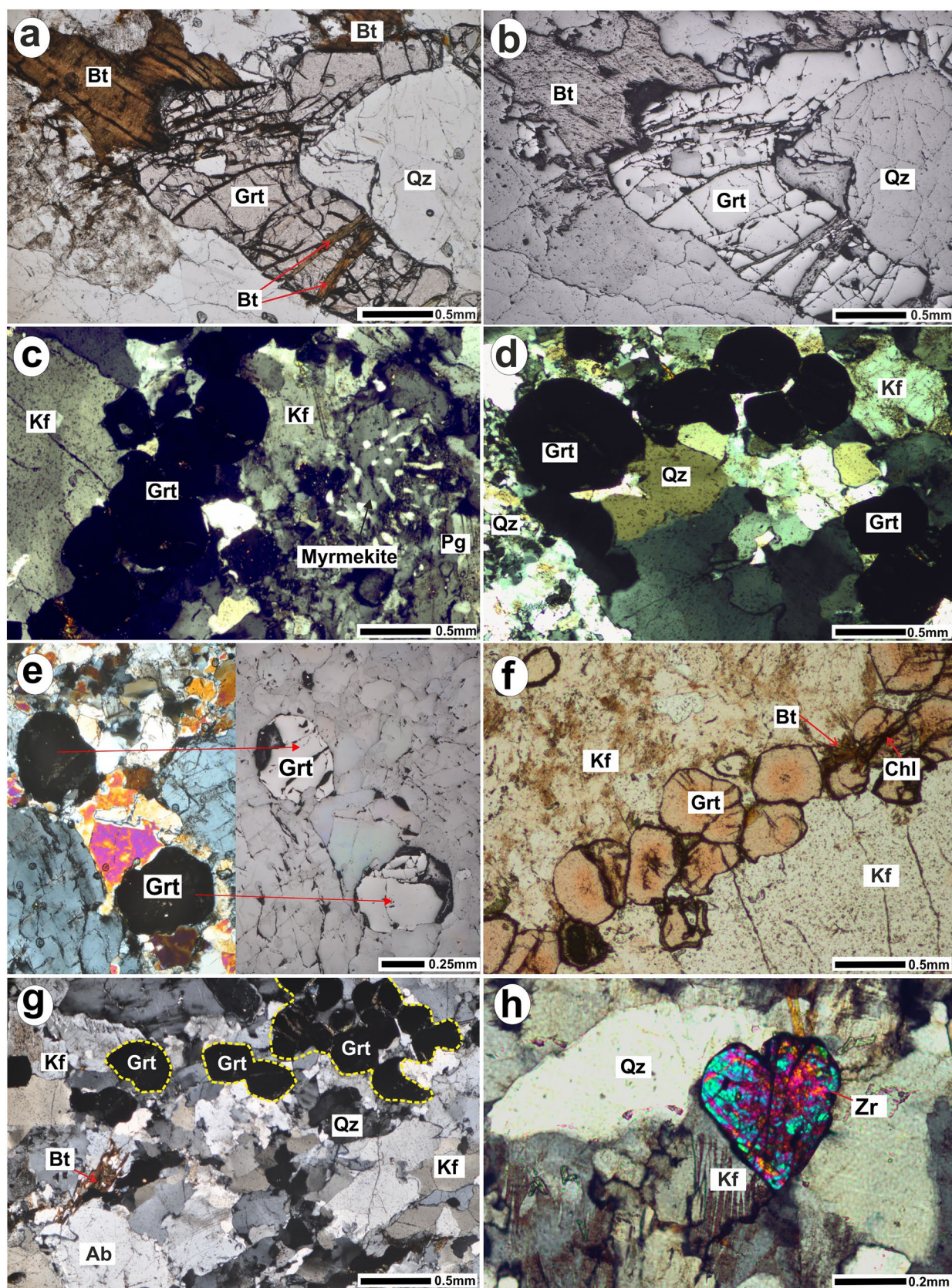


Fig. 3 Photomicrographs of Wadi El-Hima granites and associated garnets. **a, b** Anhedral to ridge shape interstitial coarse garnet (Grt) grains between quartz (Qz) crystals rimmed and veined by biotite (Bt) in garnet-bearing trondhjemites. **c** Coarse garnet crystals between alkali feldspar (Kf) and plagioclase (Pg) in garnet-rich syenogranites, exhibiting myrmekitic textures. **d** Coarse disseminated subhedral garnet grains in the interstitial space between plagioclase, K-feldspar and quartz in garnet-rich syenogranites. **e** Subhedral disseminated and homogenous garnet crystals in garnet-rich syenogranites. **f, g** High concentrations of subhedral garnet crystals occurring as vein type and grain aggregates in the interstitial space between K-feldspar in garnet-rich syenogranites. **h** Heart-shaped twinned zircon (Zr) crystal with sharp contacts with K-feldspar and quartz in alkali feldspar granites

plagioclase grains are altered to sericite. K-metasomatism has led to the rims of zoned plagioclase being partially replaced by coarse interstitial K-feldspar with myrmekite rims, which leaves small plagioclase grains behind. Quartz grains show undulose extinction and form sharp boundaries with plagioclase and garnet crystals (Fig. 3a). K-feldspar (Supplementary 2a) is represented by microcline and perthite intergrowths (band or patchy type). Perthite prismatic crystals are orthoclase or microcline, including albite threads. Garnets occur as interstitial grains with anhedral or ridge-like shapes, and are rimmed and veined by flaky biotite (Fig. 3a, b). They form homogenous, coarse crystals (2–5 mm) and are free of inclusions, except for some quartz blebs and zircon (Fig. 3a, b). Zircon occurs as inclusions in garnet and plagioclase, whereas ilmenite exists as interstitial subhedral crystals. Flaky biotite contains zircon and apatite inclusions and occurs at the rim of garnets (Fig. 3a, b). Some chlorite flakes occur along garnet and biotite rims and in microcracks.

Garnet-rich syenogranites show hypidiomorphic equigranular textures and consist mainly of K-feldspar (30–40 vol%), quartz (25–32 vol%), plagioclase (12–18 vol%), and variable concentrations of garnet (4–30 vol%) (Fig. 3c–h) with small amounts of biotite (~2 vol%) (Fig. 3g; Supplementary 1b, c). Chlorite occurs as a secondary mineral (~1 vol%) and accessory minerals include zircon, apatite, titanite, Fe–Ti oxides, allanite, monazite and leucosene (Supplementaries 1c, 2b–d). Coarse columnar crystals of K-feldspars show perthitic exsolution, while fine crystals form microcline in the groundmass. Some K-feldspar crystals replace precursor plagioclase crystals, where a remnant plagioclase occurs along K-feldspar rims (Fig. 3c). Perthite intergrowths contain thin threads of albite (Fig. 3g). Some quartz grains show undulose extinction. Plagioclase (An_{14–15}) is found as columnar crystals and few sericite grains occur along its cleavages. Some plagioclase grains have experienced metasomatism, forming minor perthite and myrmekitic textures (Fig. 3c). Biotite occurs as flakes between quartz and albite or laths in K-feldspar (Fig. 3g; Supplementary 1b, c), although sometimes shows

equilibrium textures with surrounding garnet crystals (Supplementary 1b, c). Some chlorite crystals exist as flakes, filling cracks in garnets (Fig. 3f). Fe–Ti oxides occur as individual crystals, granular aggregates or fill in fractures in garnet (Supplementary 2d). Zircon is mainly associated with garnet (Supplementary 2b, d), chlorite, ilmenite and titanite. Garnet is homogenous crystals, free of inclusions (Fig. 3e) and is slightly dissected by cracks filled with chlorite (Fig. 3f). It has three modes of occurrence: (1) subhedral disseminated crystals (0.6–1.0 mm) (Fig. 3d, e; Supplementary 2b–d), (2) vein types or clusters of subhedral crystals (Fig. 3f) and (3) aggregated subhedral (0.3–0.5 mm) to slightly rounded crystals (Fig. 3g). Few garnet crystals contain plagioclase and zircon inclusions (Supplementaries 1d, 2d), whereas monazite occurs at garnet rims (Supplementary 2c). Subhedral garnets as disseminated, vein-type and clots show sharp boundaries with triple junctions among them and against other major constituents, reflecting their magmatic origin (Fig. 3e–g; Supplementary 1d).

Alkali feldspar granites are composed of K-feldspar (55–60 vol%) and quartz (32–35 vol%), with subordinate albite (6–8 vol%) and biotite (~2 vol%) (Fig. 3h). They show hypidiomorphic granular textures. Most samples contain the accessory minerals, zircon, Fe–Ti oxides (~1 vol%), garnet (mainly 1–4 vol%, except at contact zones, where it comprises up to 8 vol%), allanite, titanite and monazite, except for sample Ad.32, which is rich in iron oxides (up to 4 vol%). K-feldspars are mainly microcline and microperthite, which shows cross-hatch twins with flame and vein-like/perthitic intergrowths. Some K-feldspar exhibits thin lamella twins (Fig. 3h). Albite forms sharp contacts with K-feldspar. Biotite occurs as large flakes interstitially between feldspar and quartz. Biotite and chlorite alter to fine grains that occur as thin interstitial veins between feldspar and quartz. Zircon occurs as euhedral to subhedral prismatic crystals and sometimes shows heart-like shapes owing to twinning (Fig. 3h).

Remote sensing data and techniques

An ASTER sensor is one of five state-of-the-art instrument sensor systems on board the Terra satellite that launched on December 18, 1999 (Abrams 2000). ASTER remote sensing Level 1B (Granule ID: AST L1B00310162004082323) imagery data was acquired on October 16, 2004, with no cloud cover (i.e. 0%). The data were geometrically corrected, and rotated to a north-up Universal Transverse Mercator (UTM) projection (<https://lpdaac.usgs.gov>). Images were pre-georeferenced to UTM zone 36 North projection using the WGS-84 datum. In this study, VNIR and SWIR data were stacked and processed using ENVI version 5.3 and ArcGIS version 10.5 software packages. The visible VNIR and SWIR bands were atmospherically corrected using the

FLAASH algorithm. Remote sensing processes and techniques were used to emphasise and discriminate different granite types, to identify major structures and pathways of hydrothermal solution transport, garnet-rich zones, outcrops of garnet-bearing granites and garnet concentrations in stream sediments in the Wadi El-Hima area (Figs. 4, 5, 6). A general flowchart for the methodology used in this study is shown in Supplementary 3.

By applying an optimum index factor (OIF) algorithm to the ASTER data (nine reflected bands VNIR-SWIR) to create an RGB composite (Chavez et al. 1982), the best resultant highest OIF ranking values of ~74.96% was found to be represented by bands (9, 8, 1) in red, green and blue (RGB) colour channels, respectively (Fig. 1b). Three granitic phases have been distinguished: garnet-bearing trondhjemites and garnet-rich syenogranites are represented by a whitish tone, and alkali feldspar granites of Gabal El-Faliq and Wadi El-Hima are represented by a dark orange tone and a greyish green tone, respectively (Fig. 1b).

The band ratio technique was prepared by dividing the digital number values of each pixel in one band by the

corresponding digital number values of another band (Drury 1993; Madani and Emam 2011). Band ratios (1/2, 4/7, 3/4) and (4/5, 1/3, 6/3) in RGB are useful for lithologic discrimination of rock units in the study area (Fig. 4a, b). Garnet-bearing trondhjemites were distinguished in band ratio composite images of (1/2, 4/7, 3/4) with a dark blue colour, whereas garnet-rich syenogranites were distinguished by a very light cyan (Fig. 4a). On the other hand, an ASTER band ratio of composite (4/5, 1/3, 6/3) in RGB (Fig. 4b) discriminated garnet-bearing trondhjemites with a bright violet colour, whereas garnet-rich syenogranites were distinguished with a vivid orange colour (Fig. 4b). Alkali feldspar granites at Wadi El-Hima have a blue colour (Fig. 4b).

Principal component analysis (PCA) displays the maximum contrast from several spectral bands with just three primary displaying colours (Vincent 1997; Sadek et al. 2015). Based on ASTER-image composites (PC6, PC4, and PC2) in RGB (Fig. 4c), tonalities and granodiorites were successfully discriminated by soft green to slightly desaturated red colours, while garnet-bearing trondhjemites were distinguished by a cyan colour. Both garnet-rich syenogranites

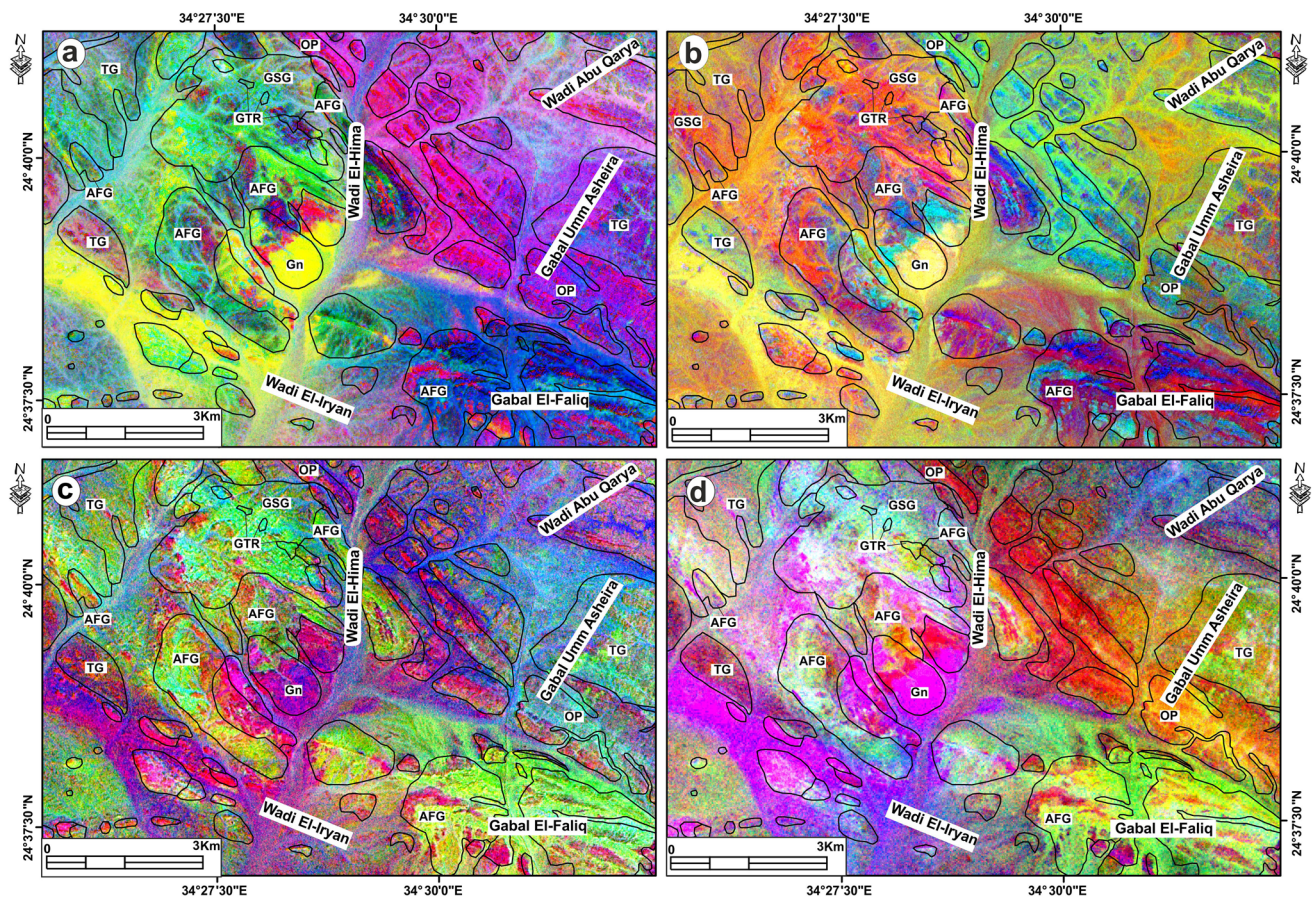


Fig. 4 Remote sensing ASTER data image techniques. **a** Band ratio composite image of (2/1, 3/4, 4/7) in RGB. **b** Band ratio composite image of (2/1, 3/4, 4/7) in RGB. **c** PCA composite image of (PC6,

PC4, PC2) in RGB. **d** PCA composite image of (PC4, PC3, PC2) in RGB. Abbreviations as in Fig. 1

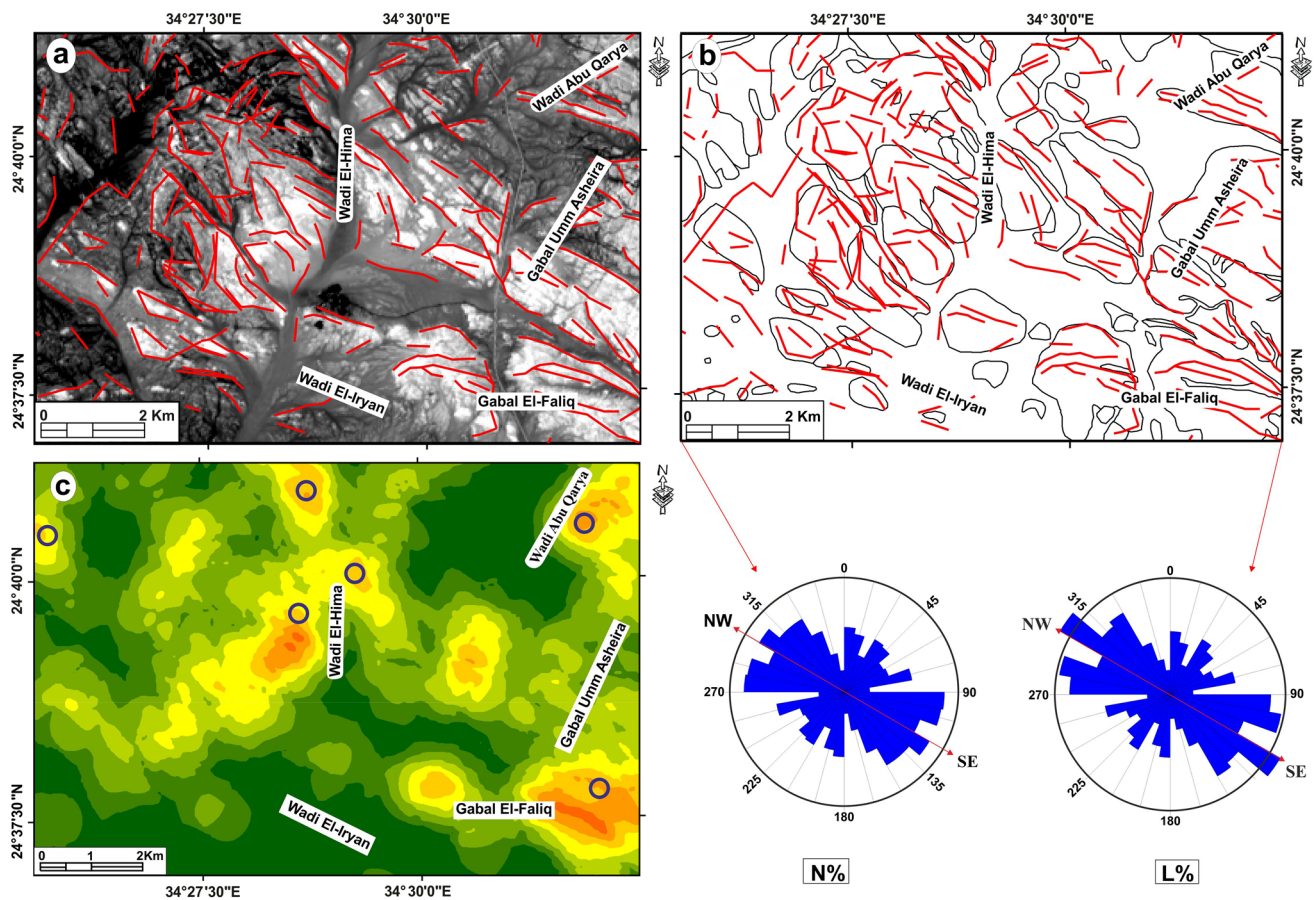


Fig. 5 Structure and density lineament maps of the Wadi El-Hima area. **a** Lineaments based on PC1 from ASTER imagery data. **b** Structure lineaments map and rose diagrams of the study area. **c** Lineaments density map of the Wadi El-Hima area

and alkali feldspar granites were discriminated into moderate dark to soft green colours in the mapped area (Fig. 4c). The PCA-image (PC4, PC3, and PC2) in RGB discriminated tonalites and granodiorites as blue and green colours, while the garnet-bearing trondhjemites were distinguished by a very light cyan colour. Garnet-rich syenogranites have a very soft magenta colour, and alkali feldspar granites show soft green to vivid orange colours (Fig. 4d).

An automatic lineaments extraction method is widely used to extract surface structure lineaments to investigate geological structure and tectonic fabrics (Hung et al. 2005). In this study, the GeoAnalyst-PCI software was used to perform an automatic lineament extraction from ASTER sensor data image of VNIR-SWIR. The first principal component represents the direction of largest data variance and largest information of surface structure features (Richards and Xiuping 2006). The PC1 of the eight-bit grayscale is suitable for structure lineament extraction in this study. The lineaments length and number percentages extracted from the ASTER data are shown in the rose diagrams (Fig. 5a, b), which reveal dominantly NW–SE-trending lineaments and secondary NNE–SW and N–S trending lineaments. The

dominant NW–SE trending lineaments (Fig. 5a, b) are parallel to the NW–SE strike of the major Najd fault system in the Eastern Desert of Egypt.

A lineament density map (Fig. 5c) was created using the interpolation process in ArcMap. In the Wadi El-Hima granites, high-density zones were found in the garnet-bearing trondhjemites (i.e. associated with pervasive metasomatism) and at the contacts between garnet-rich syenogranites and alkali feldspar granites (Fig. 5c). These higher density zones coincide with rock units characterized by faults and fractures, and these zones are generally oriented towards the north and the northwest, corresponding to the dominant strike of lineaments. Because lineaments are considered as potential pathways for fluid migration, areas with a higher density of lineaments (Fig. 5a) should be zones of mineral accumulation. Zones of blue circles on the density map (Fig. 5c), which have a NW–SE striking fault, are considered the main garnet-rich zones in the Wadi El-Hima area.

Spectral mapping techniques, which are represented by SAM and MF methods, were applied for ASTER (VNIR-SWIR) bands of the study area to map garnet compositional endmembers. ENVI's spectral analyst tool applied

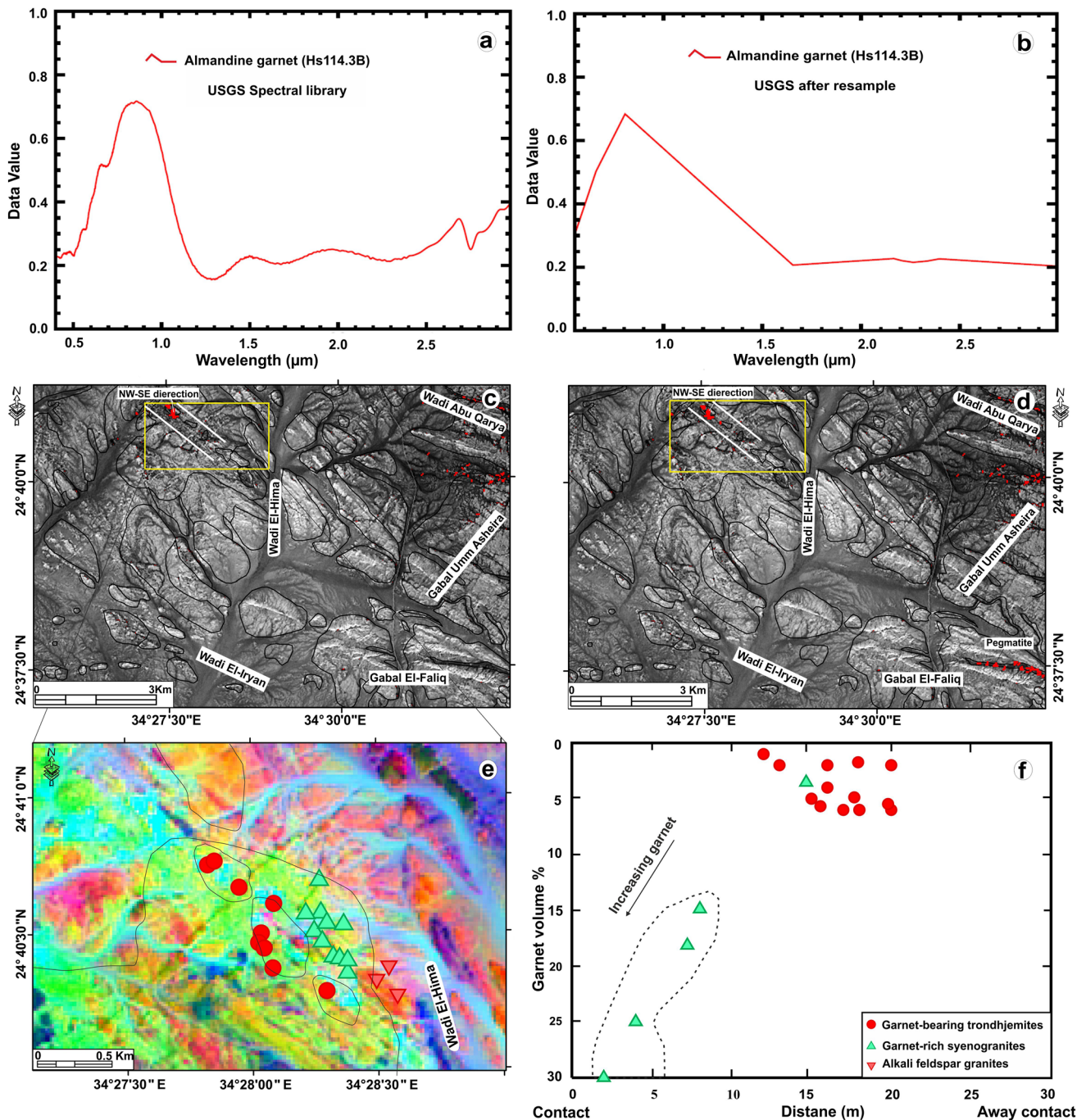


Fig. 6 Spectral remote sensing mapping techniques showing garnet distribution and accumulation in the Wadi El-Hima area. **a** Almandine-garnet spectral curve from the USGS library. **b** Almandine-garnet spectral signature after resampling. **c** Spectral angle mapper (SAM) technique showing high accumulation of garnets in Wadi El-Hima granites, Umm Asheira tonalites–granodiorites and stream sediments. **d** Matched filtering (MF) technique displaying high accumulation of garnets in Wadi El-Hima granites, Umm Asheira

tonalities–granodiorites, stream sediments and pegmatite of Gabal El-Faliq. **e** Close-up view of decorrelation stretch (7, 3, 1) in RGB to discriminate Wadi El-Hima granitic types and distribution of garnets. **f** Relation between distance (meter) from the contact with alkali feldspar granites and garnet volume percentage (vol%) in different granite types, showing increasing of garnet concentration in garnet-rich syenogranites toward the contact with alkali feldspar granites

algorithms with the aid of the USGS's spectral library (Fig. 6a) after resampling the ASTER data's spectral resolution to facilitate the matching processes (Fig. 6b). The SAM

technique (Kruse et al. 1993) depends on angles between image pixel spectra and training data (ROIs) spectra or library spectra. The result of the SAM technique is shown

in Fig. 6c, with the almandine endmember of garnet selected from the USGS library (at a threshold of 0.46). This technique revealed the highest concentration of garnet in the northwest of the mapped area, especially in trondhjemites and syenogranites (Fig. 6c). Other garnet concentrations are located in the northeastern region in Wadi stream sediments (i.e. Wadi Abu-Qarya) (Fig. 6c).

Finally, a matched filtering (MF) technique was employed to determine the abundance of garnet using a partial unmixing algorithm. MF scores indicate the degree of how well unknown pixels were matched with endmember minerals (Pour and Hashim 2012). The result of MF analysis (Fig. 6d) show the distribution of the almandine endmember of garnet (at a threshold of 0.077) in the northwest (in garnet-bearing trondhjemites and garnet-rich syenogranites), in the northeast (in stream sediments of Wadi Abu Qarya and tonalites–granodiorites), and in pegmatite dykes at Gabal El-Faliq (Fig. 6d). These results are consistent with field observations (Fig. 2), petrography (Fig. 3), and EDS analysis of mineral chemistry (Supplementaries 1, 4, 5), which indicate strong correlations between field and applied techniques. Garnet-rich zones (Fig. 6c–f) and garnet-rich granites (Fig. 1c) have a NW–SE trend (Fig. 5b) matching the Najd fault system that is dominant in the CED of Egypt and controls mineralization (e.g., Gabal Abu Dabbab after Heikal et al. 2019) in granites, for example garnet-rich zones (Fig. 6c–f) in granites from the Wadi El-Hima area.

Mineral chemistry

Major element composition

Major element compositions of feldspars, biotite, garnet, chlorite, Fe–Ti oxides, zircon, rutile, and titanite (Tables 1, 2; Supplementary 4) in I- and A-type mineralized granites were determined using an electron probe microanalyzer with a wavelength-dispersive X-ray spectrometry (JEOL JXA-8600SX) housed at Niigata University, Japan. Operating conditions comprised 15 kV accelerating voltage, 13 nA beam current, and ~1 µm beam diameter. Data were processed by using an oxide ZAF matrix correction. Fe–Ti–V oxide minerals and accessory minerals were analysed by scanning electron microscopy (SEM) energy-dispersive X-Ray spectroscopy (EDS) at Niigata University, Japan. Operating conditions were 20 kV accelerating voltage, and working distance (WD) was 10 mm. Selected electron probe microanalyzer analyses of mineral separates from stream sediments of Wadi El-Hima in the study area are listed in Supplementary 4. The analyzed minerals were garnet, amphibole, ilmenite, magnetite and titanite. Zircon and other

rare minerals (e.g. monazite, thorite and fergusonite) were identified and analyzed by SEM–EDS (Supplement 5).

Compositions of representative plagioclase and alkali feldspar in Wadi El-Hima granites (21 and 38 analysis points, respectively) are listed in Table 1 and Supplementaries 4, 6a, b. Plagioclase (An_{13-18}) in garnet-bearing trondhjemites and in garnet-rich syenogranites (An_{14-15}) is mainly oligoclase (Supplementaries 4, 6a, b), likely due to metasomatism having converted Ca-rich plagioclase in primary tonalites to Na-rich plagioclase in metasomatic trondhjemites. In contrast, plagioclase in alkali feldspar granites is mainly albite (An_{5-7}) in composition (Supplementaries 4, 6a), located near end-member $NaAlSi_3O_8$ with low K_2O (0.22 wt% on average) and CaO (0.17 wt%). K-feldspars are orthoclase with wide compositional ranges (Or_{76-98}). The orthoclase contents of K-feldspar in trondhjemites and alkali feldspar granites are the same (Or_{85-98}), but higher than orthoclase in syenogranite (Or_{76-88}) (Table 1; Supplementary 4). K-feldspar has high K_2O contents (13–17.4 wt%) in all granites, but low Na_2O (0.9 wt% on average) and CaO (0.02 wt%) contents, and plot near the sanidine end-member $KAlSi_3O_8$ (Supplementary 6b; Deer et al. 1992).

Twenty-nine analyzed points in garnet and calculated end-member mole fractions (based on 12 oxygen atoms) are listed in Table 2 and Supplementaries 4, 6c. Garnets in trondhjemites are generally homogenous, with few weakly zoned crystals. All contain high SiO_2 (37 wt%), FeO (33 wt%) and Al_2O_3 (21 wt% on average), with lesser amounts of MnO (4 wt%), CaO (2 wt%) and MgO (2 wt%). They are mainly almandine (65–82 mol%) in composition with minor spessartine (6–15 mol%), pyrope (6–16 mol%), grossular (2–15 mol%) and andradite (0–3 mol%) components. While garnets in garnet-rich syenogranites have similar almandine (67–82 mol%) with minor spessartine (8–16 mol%), pyrope (4–5 mol%), grossular (0.6–7 mol%) and andradite (0–8 mol%) components to garnet-bearing trondhjemites (Supplementary 4). On the other hand, garnets in alkali-feldspar granites are dominantly almandine (90 mol%) in composition with minor spessartine (4 mol%), pyrope (1 mol%), grossular (4 mol%) and rare andradite and uvarovite components. Finally, garnets in garnet-bearing trondhjemites have the highest pyrope (6–16 mol%) and grossular (2–15 mol%) contents but low andradite (0–3 mol%) relative to those in other granite types, while garnets in garnet-rich syenogranites have the highest spessartine (8–16 mol%) and andradite (up to 8 mol%) contents (Supplementaries 4, 6c).

On a ternary diagram of Pyr–Alm–Sps (Supplementary 6c), garnet compositions plot near the almandine end-member and within the field of magmatic almandine garnets in both Egyptian I-type granites and Umm Asheira tonalites–granodiorites (Emam et al. 2011; Moghazi et al. 2004; Thabet 2013). On the other hand, garnets in stream sediments are mainly almandine (65.6 mol%) with

Table 1 Representative electron microprobe analyses of feldspars, biotite and chlorite in Wadi El-Hima granites, Egypt

Rock name	Garnet-bearing trondhjemites										Garnet-rich syenogranites										Alkali feldspar granites											
	Plagioclase		K-feldspar		Chlorite		AD25		AD27		AD28		Plagioclase		K-feldspar		Biotite		Chlorite		Plagioclase		K-feldspar		Biotite		Chlorite					
Mineral	AD14	AD15	AD14	AD25	AD25	AD15	AD25	AD27	AD28	AD29	AD46	AD29	AD41	AD29	AD41	AD29	AD41	AD29	AD41	AD29	AD41	AD29	AD41	AD29	AD41	AD29	AD41	AD29	AD41	AD29	AD41	
Sample#	AD14	AD15	AD14	AD25	AD25	AD15	AD25	AD27	AD28	AD29	AD46	AD29	AD41	AD29	AD41	AD29	AD41	AD29	AD41	AD29	AD41	AD29	AD41	AD29	AD41	AD29	AD41	AD29	AD41	AD29	AD41	
Spot#	226	284	225	104	225	278	98	87	261	35	62	33	27	38	24	37	26	236	73	238	121	131	132	233	237	237	237	237	237	237	237	237
SiO ₂	64.66	64.73	66.32	65.38	65.38	24.84	31.45	23.07	24.81	65.23	64.85	64.25	65.88	33.79	30.84	42.41	24.25	66.48	67.26	64.27	63.84	32.40	32.89	25.96	25.79	25.79	25.79	25.79	25.79	25.79	25.79	25.79
TiO ₂	0.01	0.00	0.00	0.00	0.00	0.06	0.78	0.07	0.13	0.07	0.00	0.00	0.03	3.73	5.48	0.34	0.27	0.00	0.05	0.01	0.00	3.83	3.65	0.13	0.07	0.07	0.07	0.07	0.07	0.07	0.07	0.07
Al ₂ O ₃	23.23	23.02	19.35	18.68	18.68	22.81	21.36	22.23	22.14	21.84	22.46	18.76	18.41	16.72	16.77	16.62	20.70	21.77	21.43	18.80	19.27	17.15	17.65	19.71	16.81	16.81	16.81	16.81	16.81	16.81	16.81	16.81
Cr ₂ O ₃	0.03	0.00	0.01	0.00	0.00	0.00	0.03	0.00	0.00	0.00	0.00	0.00	0.00	0.00	0.04	0.00	0.07	0.00	0.06	0.07	0.02	0.03	0.01	0.01	0.03	0.03	0.03	0.03	0.03	0.03	0.03	0.03
FeO ^a	0.00	0.03	0.08	0.06	0.06	37.72	26.44	36.85	36.67	0.02	0.00	0.09	0.02	29.66	31.61	21.21	38.87	0.11	0.06	0.07	0.08	33.28	33.48	39.20	39.60	39.60	39.60	39.60	39.60	39.60	39.60	39.60
MnO	0.00	0.00	0.00	0.01	0.00	1.39	0.96	2.00	1.57	0.02	0.01	0.00	0.00	0.32	0.16	0.05	0.22	0.05	0.00	0.08	0.00	0.05	0.09	0.25	0.58	0.58	0.58	0.58	0.58	0.58	0.58	0.58
MgO	0.00	0.00	0.00	0.00	0.00	4.83	8.70	4.55	5.09	0.00	0.00	0.00	0.00	3.65	2.39	2.01	3.67	0.00	0.01	0.00	0.00	0.15	0.02	3.10	3.38	3.38	3.38	3.38	3.38	3.38	3.38	3.38
CaO	3.41	3.37	0.04	0.07	0.00	0.03	0.75	0.00	0.04	3.00	2.98	0.03	0.02	0.04	0.21	3.94	0.04	1.11	1.35	0.00	0.00	0.01	0.01	0.09	0.19	0.19	0.19	0.19	0.19	0.19	0.19	0.19
Na ₂ O	8.74	9.44	0.45	1.40	1.40	0.02	0.02	0.01	0.00	9.71	9.95	0.50	1.43	0.08	0.11	0.34	0.06	10.58	10.11	0.49	0.71	0.03	0.05	0.03	0.05	0.05	0.05	0.05	0.05	0.05	0.05	0.05
K ₂ O	0.08	0.28	14.11	14.87	14.87	0.00	0.74	0.00	0.04	0.06	0.24	16.74	15.32	9.25	5.87	1.56	0.00	0.19	0.26	16.54	16.02	9.35	9.44	0.00	0.00	0.00	0.00	0.00	0.00	0.00	0.00	0.00
NiO	0.02	0.03	0.03	0.00	0.00	0.00	0.00	0.00	0.00	0.01	0.00	0.00	0.00	0.00	0.00	0.00	0.00	0.00	0.00	0.00	0.00	0.00	0.06	0.03	0.00	0.00	0.00	0.00	0.00	0.00	0.00	0.00
BaO	0.06	0.13	0.00	0.00	0.00	0.00	0.09	0.07	0.00	0.13	0.00	0.13	0.00	0.00	0.02	0.00	0.03	0.00	0.00	0.18	0.25	0.06	0.02	0.00	0.11	0.11	0.11	0.11	0.11	0.11	0.11	0.11
Total	100.2	101.0	100.4	100.5	100.5	91.70	91.3	88.8	90.5	100.1	100.5	100.5	101.1	97.2	93.5	88.5	88.2	100.3	100.6	100.5	100.2	96.34	97.36	88.51	86.62	86.62	86.62	86.62	86.62	86.62	86.62	86.62
End-members (mol%)																																
An	17.67	16.23	0.22	0.36	0.36	–	–	–	–	14.54	14.01	0.14	0.09	–	–	–	–	5.41	6.78	0.00	0.00	–	–	–	–	–	–	–	–	–	–	–
Ab	81.87	82.18	4.63	12.50	12.50	–	–	–	–	85.11	84.62	4.33	12.40	–	–	–	–	93.48	91.65	4.33	6.32	–	–	–	–	–	–	–	–	–	–	–
Or	0.46	1.60	95.15	87.14	87.14	–	–	–	–	0.35	1.37	95.53	87.51	–	–	–	–	1.12	1.57	95.67	93.68	–	–	–	–	–	–	–	–	–	–	–
Mg#	–	–	–	–	–	0.37	0.33	0.17	0.20	–	–	–	–	0.18	0.12	0.14	0.14	–	–	–	–	0.01	0.00	0.12	0.13	0.13	0.13	0.13	0.13	0.13	0.13	0.13
Fe#	–	–	–	–	–	0.63	0.67	0.83	0.80	–	–	–	–	0.82	0.88	0.86	0.86	–	–	–	–	0.99	1.00	0.88	0.87	0.87	0.87	0.87	0.87	0.87	0.87	0.87

^aTotal iron given as FeO; An: anorthite, Ab: albite, Or: orthoclase. Mg# = (Mg/Mg+Fe); Fe# = (Fe/Fe+Mg)

Table 2 Representative electron microprobe analyses of garnets in Wadi El-Hima granites, Egypt

Rock N	Garnet-bearing trondhjemites										Garnet-rich syenogranites										Alkali gran- ites																																																																																																																																																																																																																																																																																																																																																																																																																																																																																																																																																																																																																																																						
	AD14					AD15					AD25					AD27					AD28					AD30					AD39					AD41					AD46					AD37																																																																																																																																																																																																																																																																																																																																																																																																																																																																																																																																																																																																																													
	Core		Rim			Core		Rim			Core		Rim			Core		Rim			Core		Rim			Core		Rim			Core		Rim		Core		Rim																																																																																																																																																																																																																																																																																																																																																																																																																																																																																																																																																																																																																																						
Sample#	AD14		AD14			AD15		AD15			AD25		AD25			AD27		AD27			AD28		AD28			AD30		AD30			AD39		AD39			AD41		AD41			AD46		AD46		AD37		AD37																																																																																																																																																																																																																																																																																																																																																																																																																																																																																																																																																																																																																												
Mode	Dissiminated		Dissiminated			Dissiminated		Dissiminated			Dissiminated		Dissiminated			Dissiminated		Dissiminated			Dissiminated		Dissiminated			Dissiminated		Dissiminated			Dissiminated		Dissiminated			Dissiminated		Dissiminated			Dissiminated		Dissiminated																																																																																																																																																																																																																																																																																																																																																																																																																																																																																																																																																																																																																																
Texture	Core		Rim			Core		Rim			Core		Rim			Core		Rim			Core		Rim			Core		Rim			Core		Rim			Core		Rim			Core		Rim																																																																																																																																																																																																																																																																																																																																																																																																																																																																																																																																																																																																																																
Spot#	229	231	280	281		101	102	85	86		263	264	51	52		55	255	34	19		21	22		61	66		22	21		34	19		21	22		61	66		22	21		34	19		21	22																																																																																																																																																																																																																																																																																																																																																																																																																																																																																																																																																																																																																													
SiO ₂	37.42	37.22	37.03	36.78		37.46	37.28	37.65	37.48		37.18	37.16	36.77	36.96		37.43	36.61	37.15	36.61		37.61	36.87		37.18	37.51		37.61	36.87		37.15	36.61		37.61	36.87		37.18	37.51		37.61	36.87		37.18	37.51		37.61	36.87																																																																																																																																																																																																																																																																																																																																																																																																																																																																																																																																																																																																																													
TiO ₂	0.01	0.00	0.00	0.04		0.00	0.00	0.01	0.00		0.04	0.00	0.02	0.00		0.02	0.00	0.00	0.00		0.00	0.00		0.00	0.00		0.00	0.00		0.00	0.00		0.00	0.00		0.00	0.00		0.00	0.00		0.00	0.00																																																																																																																																																																																																																																																																																																																																																																																																																																																																																																																																																																																																																																
Al ₂ O ₃	21.31	21.16	21.15	21.35		21.27	21.39	20.36	20.25		20.91	21.38	21.20	21.29		21.32	20.89	18.57	18.81		19.69	19.48		20.97	20.73		19.69	19.48		18.57	18.81		19.69	19.48		20.97	20.73		20.97	20.73		20.97	20.73																																																																																																																																																																																																																																																																																																																																																																																																																																																																																																																																																																																																																																
Cr ₂ O ₃	0.06	0.00	0.00	0.05		0.00	0.00	0.01	0.00		0.04	0.05	0.00	0.00		0.03	0.05	0.03	0.03		0.00	0.00		0.04	0.04		0.00	0.00		0.03	0.03		0.00	0.00		0.04	0.04		0.04	0.04																																																																																																																																																																																																																																																																																																																																																																																																																																																																																																																																																																																																																																			
FeO ^a	33.00	34.24	35.90	35.55		33.44	33.86	32.89	33.38		32.73	32.91	33.12	30.58		29.83	35.00	33.01	33.52		35.82	37.34		35.98	36.25		37.34	35.82		33.01	33.52		35.82	37.34		35.98	36.25		37.34	35.82		35.98	36.25																																																																																																																																																																																																																																																																																																																																																																																																																																																																																																																																																																																																																																
MnO	2.93	3.88	2.49	2.50		2.75	3.19	5.36	5.24		4.41	4.61	6.42	4.39		4.10	6.12	6.76	6.76		3.55	4.26		3.84	4.00		4.26	3.55		6.12	6.76		3.55	4.26		3.84	4.00		4.26	3.55		3.84	4.00																																																																																																																																																																																																																																																																																																																																																																																																																																																																																																																																																																																																																																
MgO	2.05	1.78	2.06	2.13		4.11	3.15	2.20	2.36		2.19	2.34	1.99	2.26		2.38	1.52	1.26	0.93		1.05	0.96		1.08	1.07		1.05	0.96		1.26	0.93		1.05	0.96		1.08	1.07		1.08	1.07																																																																																																																																																																																																																																																																																																																																																																																																																																																																																																																																																																																																																																			
CaO	3.92	1.73	1.43	1.38		1.12	1.22	1.67	1.20		2.70	1.61	1.52	4.14		5.49	2.07	4.21	4.14		3.55	1.70		1.76	1.47		3.55	1.70		4.21	4.14		3.55	1.70		1.76	1.47		1.76	1.47																																																																																																																																																																																																																																																																																																																																																																																																																																																																																																																																																																																																																																			
NiO	0.00	0.00	0.02	0.05		0.04	0.04	0.01	0.00		0.00	0.08	0.00	0.07		0.00	0.01	0.00	0.00		0.00	0.02		0.00	0.02		0.00	0.00		0.00	0.00		0.00	0.02		0.00	0.02		0.00	0.02																																																																																																																																																																																																																																																																																																																																																																																																																																																																																																																																																																																																																																			
BaO	0.00	0.00	0.00	0.00		0.02	0.02	0.06	0.04		0.00	0.00	0.00	0.03		0.01	0.00	0.00	0.00		0.05	0.00		0.00	0.00		0.05	0.00		0.00	0.00		0.05	0.00		0.00	0.00		0.00	0.00																																																																																																																																																																																																																																																																																																																																																																																																																																																																																																																																																																																																																																			
Total	100.7	100.0	100.1	99.8		100.2	100.1	100.2	99.9		100.2	100.1	101.0	100.2		100.9	100.2	100.4	100.8		101.3	100.6		100.8	101.1		100.6	101.3		100.4	100.8		100.8	101.3		100.8	101.1		100.8	101.1																																																																																																																																																																																																																																																																																																																																																																																																																																																																																																																																																																																																																																			
Mg#	0.10	0.08	0.09	0.10		0.18	0.14	0.11	0.11		0.11	0.11	0.10	0.12		0.13	0.07	0.07	0.05		0.05	0.05		0.05	0.05		0.05	0.05		0.07	0.05		0.05	0.05		0.05	0.05		0.05	0.05																																																																																																																																																																																																																																																																																																																																																																																																																																																																																																																																																																																																																																			
Fe#	0.90	0.92	0.91	0.90		0.82	0.86	0.89	0.89		0.89	0.89	0.90	0.88		0.87	0.93	0.93	0.95		0.95	0.95		0.95	0.95		0.95	0.95		0.93	0.95		0.95	0.95		0.95	0.95																																																																																																																																																																																																																																																																																																																																																																																																																																																																																																																																																																																																																																						
End-members (mol%)																																																																																																																																																																																																																																																																																																																																																																																																																																																																																																																																																																																																																																																																											

spessartine (16.4 mol%), pyrope (12 mol%), grossular (5 mol%) and minor andradite (1.3 mol%) components and are similar in chemical composition to garnets in the Wadi El-Hima granites (Table 2; Supplementary 4).

Biotite in garnet-rich syenogranites and alkali feldspar granites (Table 1; Supplementary 4) has 17.3 wt% Al_2O_3 , 31.4 wt% FeO, 1.3 wt% MgO, and 8.9 wt% K_2O on average. Based on a biotite discrimination diagram (Nachit et al. 2005), biotite compositions plot in the field of primary biotite (Supplementary 6d). These compositions resemble Mg- and Al-bearing annites (Deer et al. 1992) and are peraluminous (Abdel-Rahman 1994), suggesting that biotite parental magma had a peraluminous nature (Supplementary 6e). Biotite has a high Al-content (3.3–3.9 mol%) and an Fe/(Fe + Mg) ratio that ranges from 0.8 to 1.0. High-Al biotite is characteristic of I-type granites crystallized from peraluminous magmas (e.g., Dahlquist et al. 2007).

Chlorite in the studied granites has a significant amount of FeO (34 wt% on average), Al_2O_3 (21 wt%) and MgO (5 wt%) (Table 1; Supplementaries 4, 6f), indicating that it likely has a secondary origin and was derived from the breakdown of garnet or biotite. According to the classification diagram of Hey (1954), the studied chlorite has a composition of diabantite, brunsvigite and ripidolite (Supplementary 6f). Some prismatic zircon (ZrO_2) grains (Supplementary 2f) in stream sediments are characterized by bipyramidal terminations and contain significant concentrations of radioactive minerals such as thorite (ThSiO_4), uranothorite ($\text{Th, U}\text{SiO}_4$) and fergusonite ($\text{Y, REE}\text{NbO}_4$) (Supplementary 2f), as confirmed by EDS data and peaks (Supplementary 5a). Amphibole in stream sediments is edenite in composition (Leake et al. 1997). Stream sediments also contain high concentrations of monazite ($\text{Nd, Ce, La, Th}\text{(P, Si)O}_4$) and titanomagnetite (Supplementaries 2f, 5a).

Trace and rare earth elements

Trace-element concentrations of feldspar, biotite and garnet (Table 3) in garnet-rich syenogranites were determined in situ by laser ablation-inductively coupled plasma-mass spectrometry (LA-ICP-MS) using a quadrupole ICP-MS (Agilent 7500a) coupled to a 213 nm Nd:YAG laser ablation system (New Wave Research UP213) at Niigata University, Japan. Analyses were carried out by ablating 50 to 80- μm diameter spots at 4 Hz with an energy density of 10 J/cm² per pulse. The total time of data acquisition for one spot was 105 s, including laser ablation for 45 s and analysis of the background before and after for 40 s each. CaO and SiO_2 contents of silicates, and Al_2O_3 , Fe_2O_3 and TiO_2 contents of oxides determined by electron microprobe were used as an internal standard for quantification of silicates and iron oxides. SRM 612 and SRM 610 (Pearce et al. 1997) were

used as external standards for calibration of trace element concentrations.

Subhedral disseminated garnets in syenogranites are rich in heavy rare earth elements (HREE = 1636 ppm on average) contents and Y (3394 ppm), but are depleted in light rare earth elements (LREE = 11 ppm) and Eu (0.5 ppm) with very low LREE/HREE and $(\text{La/Yb})_N$ ratios. They have a very low concentration of Nb (≤ 0.5 ppm), and Ta (≤ 0.07 ppm) with slightly low and variable Zr (0.95–36.6 ppm). They have significant amounts of Zn (325 ppm), Li (39 ppm) and Ga (35 ppm). Chondrite-normalized REEs (Sun and McDonough 1989) of El-Hima garnets show strong enrichment in HREE, with slightly negative Eu anomalies (Fig. 7a), similar to magmatic garnet (Zhou et al. 2017; Sami et al. 2020), but different to hydrothermal garnet (Fig. 7a). In general, primitive mantle (PM)-normalized patterns show depletion in large ion lithophile elements (LILE) with low concentrations of Ba, Nb and Sr (Fig. 7b). This is due to the large ionic radii of these elements compared to the octahedral coordination of the garnet crystal structure (Gaspar et al. 2008).

Oligoclase contains high concentrations of LREE (53 ppm), Sr (114 ppm), Ba (42.3 ppm), Ga (44.2 ppm), Li (19 ppm) and Pb (16 ppm), but low HREE (3.4 ppm), Nb (0.03 ppm) and Ta (0.01 ppm). Albite has very low concentrations of trace elements and REE (Table 3). Chondrite-normalized REE patterns of oligoclase display LREE enrichment patterns with clear positive Eu anomalies (Fig. 8a). Based on PM normalization (Sun and McDonough 1989), oligoclase is enriched in LILE (Cs, Pb, Rb, Ba, U, Sr, and Eu), but depleted in high field strength elements (HFSE: Th, Nb, Ta and Zr) (Fig. 8b). Chondrite-normalized REEs of albite show flat patterns with positive Eu anomalies (Fig. 8a), while its PM-normalized trace elements exhibit flat spider patterns with strong positive peaks at Pb and U (Fig. 8b).

Biotite has high-average Zn (278 ppm) and Nb (56 ppm) contents, and high LREE/HREE (4.46) and $(\text{La/Yb})_N$ (23.64) ratios. Chondrite-normalized REE patterns of biotite are flat (Fig. 8c) with slightly negative Eu anomalies. These REE patterns resemble those of magmatic biotite, but differ from metamorphic biotite (Samadi et al. 2021) (Fig. 8c). PM-normalized trace element patterns of biotite show enrichment in Nb, Ta and LILE (Cs, Rb, Ba, Pb, U), but depletion in Th, Sr and Zr (Fig. 8d).

Whole-rock chemistry

Ten rock samples of Wadi El-Hima granitic varieties were selected for major, trace and rare earth element (REE) analyses. We select fresh and homogenous granite samples with less garnet concentrations (mainly less than 6 vol% of garnets) for whole-rock chemistry. XRF and ICP-MS analyses are carried out at the GeoAnalytical Lab, Washington

Table 3 Representative LA-ICP-MS of plagioclase, biotite and garnet in garnet-rich syenogranites

Sample#	Ad.29					
Mineral name	Plagioclase		Biotite		Garnet	
Lazer point	#012	#014	#011	#015	#013	#016
Li	19.04	0.03	115.03	72.56	35.33	43.01
B	1.51	0.01	0.25	0.32	0.49	0.30
Sc	0.77	0.00	4.58	3.16	82.33	86.52
V	0.05	0.01	4.67	5.12	2.69	4.26
Cr	d.i	0.01	0.79	0.48	0.22	1.99
Co	0.02	0.00	0.61	0.61	1.56	1.64
Ni	0.50	0.00	0.49	1.29	d.i	0.02
Zn	14.16	0.01	177.47	379.05	312.15	338.17
Ga	44.17	0.01	10.46	11.14	33.32	36.55
Rb	7.26	0.14	91.12	88.10	0.32	0.28
Sr	113.98	0.35	0.86	5.84	0.18	0.10
Y	1.73	0.01	3.48	9.86	3427.98	3359.99
Zr	0.93	0.14	0.29	0.06	0.95	36.62
Nb	0.03	0.00	61.05	50.27	0.39	0.50
Cs	0.05	0.00	1.31	2.98	0.00	d.i
Ba	42.26	1.02	26.33	32.97	0.03	0.00
Hf	0.04	0.00	0.01	0.00	0.08	0.94
Ta	0.01	0.00	3.82	2.16	0.14	0.07
Pb	15.94	0.02	3.25	2.01	0.04	0.04
Th	0.02	0.00	0.00	0.00	0.00	0.02
U	0.06	0.00	0.45	0.05	0.02	0.12
La	16.48	0.01	10.80	3.66	0.02	0.03
Ce	8.90	0.01	10.34	2.00	0.04	0.07
Pr	4.28	0.00	1.45	1.38	0.05	0.04
Nd	16.62	0.01	6.27	7.53	1.07	1.14
Sm	4.00	0.00	1.88	3.33	8.57	9.86
Eu	2.52	0.00	0.13	0.16	0.50	0.49
Gd	2.25	0.00	1.99	4.30	81.44	92.57
Tb	0.20	0.00	0.34	0.63	37.93	42.61
Dy	0.70	0.00	1.44	2.63	417.55	451.29
Ho	0.05	0.00	0.16	0.35	118.98	117.34
Er	0.10	0.00	0.30	0.67	428.97	363.51
Tm	0.01	0.00	0.03	0.08	69.50	52.59
Yb	0.07	0.00	0.18	0.33	516.22	363.24
Lu	0.01	0.00	0.02	0.05	71.41	47.61
Σ HREE	3.39	0.00	4.46	9.04	1742.01	1530.75
Σ LREE	52.80	0.03	30.86	18.07	10.23	11.62
Σ LREE/ Σ HREE	15.55	7.10	6.92	2.00	0.01	0.01
(La/Yb) N^a	153.02	10.83	39.73	7.55	0.00	0.00
(La/Gd) N^a	6.15	5.86	4.56	0.72	0.00	0.00
(Gd/Yb) N^a	24.88	1.85	8.72	10.55	0.13	0.21

^aNormalized to chondrite values of (Sun and McDonough 1989); (d.i) mean not detected

State University (WSU), USA. An agate-grinding bowl was used to crush each sample into homogenized pebble-sized particles, and subsequently pulverized. The concentrations of major elements and some trace elements were determined via X-ray fluorescence using a ThermoARL

XRF Spectrometer. Each powdered sample was weighed, mixed with two parts di-lithium tetraborate flux, fused at 1000 °C in a muffle furnace, and cooled. The resulting bead was reground, re-fused, and polished on a diamond lap to produce a smooth, flat surface for analysis. The

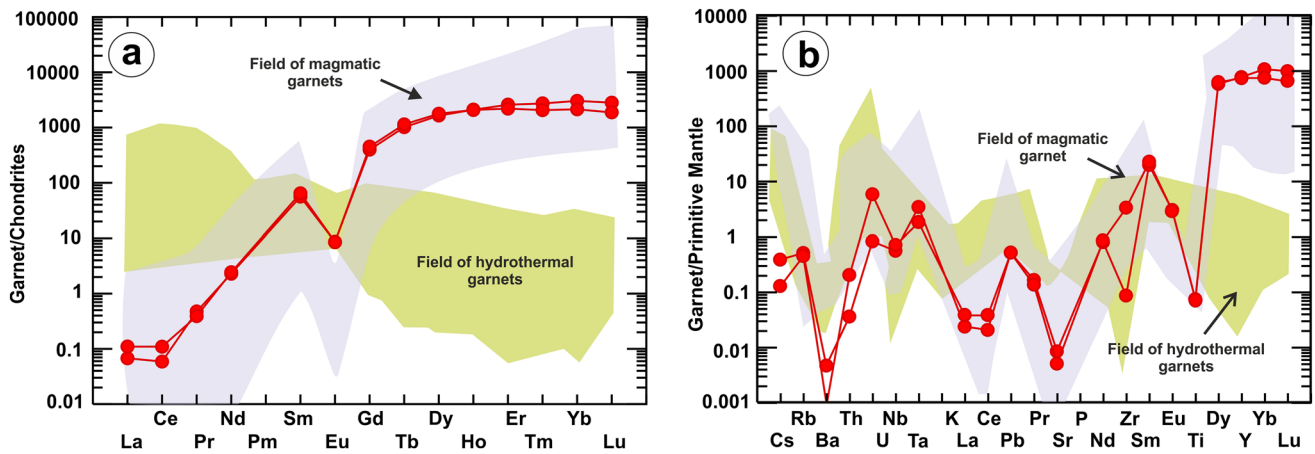


Fig. 7 In situ analyses of garnets for REE and trace elements. **a** Chondrite normalized REE patterns of disseminated garnets in garnet-rich syenogranites. **b** Primitive mantle normalized trace-element patterns of garnets in garnet-rich syenogranites. Fields of magmatic

and hydrothermal garnets (Zhou et al. 2017 and references therein) are used for comparison. REE and trace elements of garnets were normalized to chondrite and primitive mantle values, respectively (Sun and McDonough 1989)

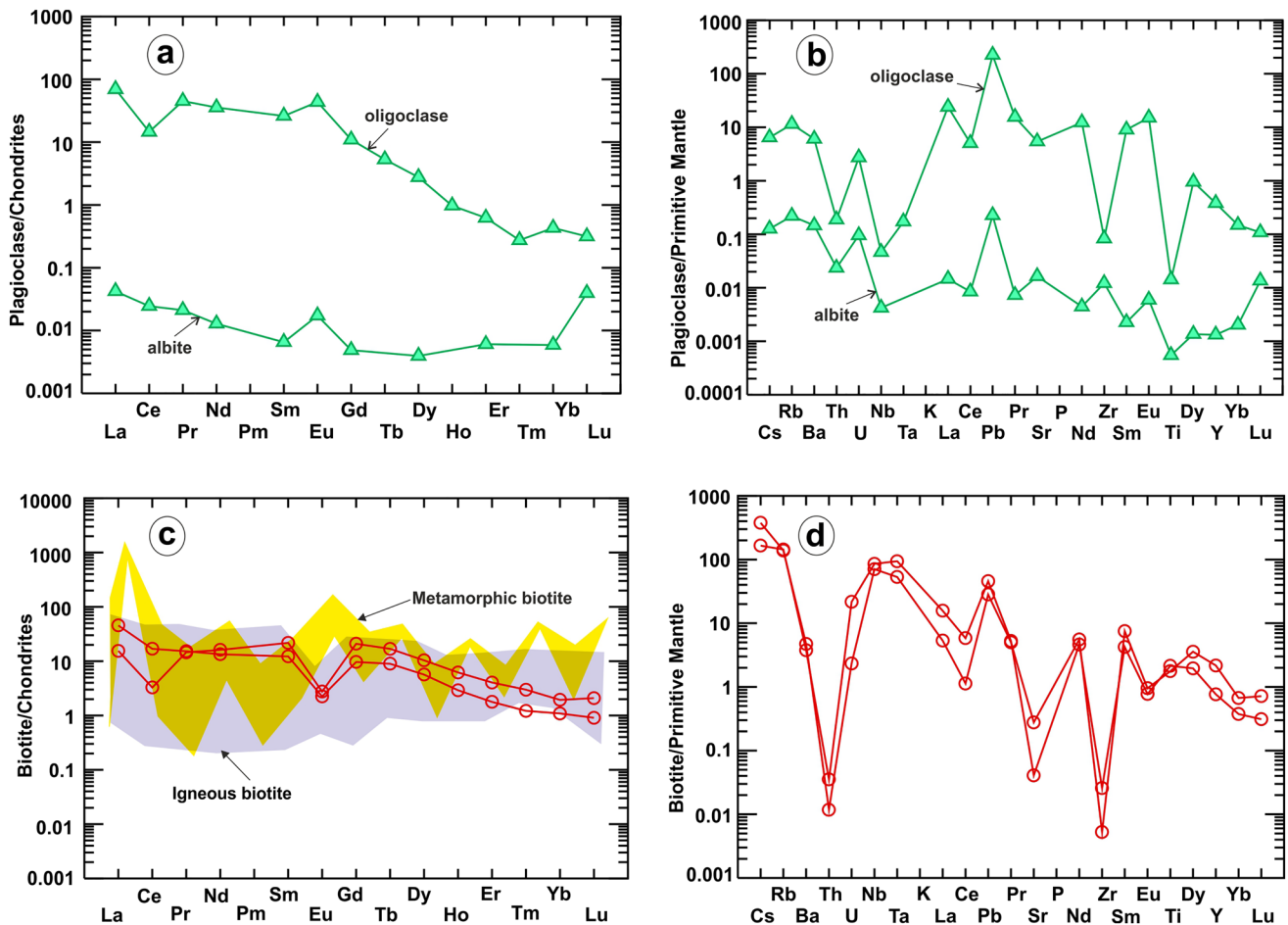


Fig. 8 In-situ analyses of plagioclase and biotite for REE and trace elements. **a** Chondrite-normalized REE patterns of plagioclase in garnet-rich syenogranites. **b** Primitive mantle normalized trace-element patterns of plagioclase. **c** Chondrite-normalized REE patterns of biotite in garnet-rich syenogranites. The fields of igneous and metamor-

phic biotite are from Samadi et al. (2021). **d** Primitive mantle normalized trace-element patterns of biotite. REE and trace elements of garnets were normalized to chondritic and primitive mantle values, respectively (Sun and McDonough 1989)

calibration standard was the reference material 650 CC from the USGS standard rock powder GSP2. The detection limit for major oxides and trace elements is available online from the GeoAnalytical Lab. The loss on ignition (LOI) was determined by the weight difference after ignition at 1000 °C.

Concentrations of REE and some trace elements were determined via ICP mass spectrometry (Agilent 7700 ICP-MS). About 50 mg powder of each sample was dissolved in acid-washed Teflon containers by refluxing in hot (250 °C) 3:1 nitric and hydrofluoric acid for at least 8 h. A working curve for instrument sensitivity was developed using a blank fused bead from the same batch of flux as used to prepare the unknowns along with USGS standards AGV-2 and RGM2. Additional USGS standards (DTS-2, BCR-1, G-2) were used as a reference for quality controlling.

The analyzed Wadi El-Hima granites are rich in SiO₂, but have a narrow range of 73.5–77.24 wt% (Table 4). Garnet-bearing trondhjemites have slightly higher SiO₂ (73.5–75.34 wt%), Na₂O (4.46–5.1 wt%) and K₂O (1.7–4.2 wt%), but lower Fe₂O₃ (0.2–0.66 wt%), CaO (1.46–2.0 wt%) and MgO as well as TiO₂ (<0.1 wt%) contents than the average compositions of the continental crust (Rudnick and Fountain 1995; Table 4). Both have the same Al₂O₃ (14.67–15.3 wt%) contents. Garnet-bearing trondhjemites are rich in Na₂O contents due to abundant oligoclase, suggesting modification of Ca-rich plagioclase by Na-metasomatism to form Na-rich plagioclase. Additionally, they have high K₂O (up to 4.2 wt%; Table 4), indicating K-metasomatism followed Na-metasomatism. Whereas garnet-rich syenogranites have similar compositions to garnet-bearing trondhjemites, except for high FeO_t (1.36–2.22 wt%) and K₂O (3.6–4.7 wt%) contents, but low Al₂O₃ (13.42–14.0 wt%) contents. Alkali-feldspar granites have the highest SiO₂ contents (75.83–77.24 wt%), with moderate Al₂O₃ (11.34–12.92 wt%), but low TiO₂ (0.02–0.13 wt%) and CaO (0.37–0.81 wt%) compared to other granites. The total alkali contents (Na₂O + K₂O) in both garnet-bearing trondhjemites (6.7–8.67 wt%) and garnet-rich syenogranites (7.57–8.44 wt%) are similar, reflecting the influence of alkali metasomatism in both types (Table 4). However, garnet-bearing trondhjemites have a lower K₂O/Na₂O ratio (0.5 on average) than the garnet-rich syenogranites (1.1). Garnet-bearing trondhjemites (Table 4) are low in LILE (e.g., Ba, Sr and Th), HFSE (e.g., Nb, Zr) as well as transition metals (e.g., Zn, V, Ni and Sc). They also show low REE contents (ΣREE = 319.4 ppm) relative to garnet-rich syenogranites (ΣREE = 319.4 ppm) and alkali feldspar granites (ΣREE = 298 ppm). On the other hand, garnet-rich syenogranites and alkali feldspar granites display enrichment of HFSE (Zr, Nb), Y (142–116 ppm), Ga (23–32 ppm) and Rb (115–88 ppm), and depletion of Sr (66–26 ppm) and transition metals (e.g., Ni, Sc, V; Table 4). The analyzed granites are peraluminous (molar A/CNK: Al₂O₃/

(CaO + Na₂O + K₂O) > 1), except one sample of alkali feldspar granite, which is metaluminous (Table 4).

On an R1–R2 classification diagram (De la Roche et al. 1980), garnet-bearing trondhjemites lie along the boundary between granodiorites and monzogranites (Supplementary 7a). Garnet-rich syenogranites and alkali feldspar granites lie in the field of syenogranite and alkali feldspar granite, respectively (Supplementary 7a). In addition, El-Hima garnet-bearing trondhjemites plot in the field of trondhjemites, where garnet-rich syenogranites and alkali feldspar granites lie in the granite field (Supplementary 7b) (Barker 1979).

Chondrite-normalized (Sun and McDonough 1989) REE patterns of garnet-bearing trondhjemites (Fig. 9a) show two types of patterns with wide ranges of Eu/Eu* (0.37–1.44; Table 4); one displays enrichment of HREE relative to LREE with a negative Eu anomaly, and the other displays slight enrichment of LREE relative to HREE with a positive Eu anomaly, similar to those of I-type trondhjemites from the ANS (Eliwa et al. 2014). In contrast, garnet-rich syenogranites and alkali feldspar granites (Fig. 9b) exhibit parallel patterns with a negative Eu anomaly (Eu/Eu* = 0.3–0.47) and resemble REE patterns of A-type granites (Sami et al. 2017). The low (La/Yb)_N ratio (0.5–2.71; Table 4) of Wadi El-Hima garnet-bearing trondhjemites and garnet-rich syenogranites is due to abundance of garnet (2–30 vol%) that is the main host of HREE (Gromet and Silver 1983). PM-normalized trace elements (Sun and McDonough 1989) for Wadi El-Hima granites exhibit slightly different patterns (Fig. 9c, d): garnet-bearing trondhjemites are rich in LILE (Cs, Rb, Th, U, K and Sr) relative to HFSE (Ta, Nb, Ti), but garnet-rich syenogranites and alkali feldspar granites are rich in HFSE (Nb and Zr), and poor in Ba, Sr, P and Ti (Fig. 9d).

Discussion

Identification of garnet-rich zones and structure lineaments using remote sensing techniques

Band ratio composites (1/2, 4/7, 3/4; Fig. 4a) and principal component composite images (PC4, PC3, and PC2; Fig. 4d) allow accurate discrimination of garnet-bearing trondhjemites from garnet-rich syenogranites. PCA composite (PC6, PC4, and PC2) successfully discriminated tonalites–granodiorites and alkali feldspar granites from ophiolitic rocks and gneisses (Fig. 4c). Band ratios and PCA techniques simply discriminated gneisses, ophiolitic rocks, alkali feldspar granites, and tonalites–granodiorites from garnet-bearing granites (trondhjemites and syenogranites); therefore, these techniques are suitable to remotely identify mineralized granites, especially garnet-rich zones (Fig. 4a–d).

Table 4 Representative chemical analysis (Major, trace and REEs) of Wadi El-Hima granites, Egypt

Rock type	Garnet-bearing trondhjemites					Garnet-rich syenogranites				Alkali feldspar granites				C.C ^a	
	Sample#	Ad15	Ad25	Ad30	Ad39	Average	Ad.29	Ad41	Ad46	Average	Ad.1	Ad10	Ad32		Average
SiO ₂	74.01	74.54	75.34	73.49	73.49	74.35	75.12	74.18	73.66	74.32	75.76	75.83	77.24	76.28	59.1
TiO ₂	0.00	0.00	0.00	0.06	0.06	0.02	0.06	0.03	0.05	0.05	0.04	0.02	0.13	0.06	0.7
Al ₂ O ₃	15.27	15.17	14.67	15.18	15.18	15.07	13.42	13.84	14.05	13.77	12.92	12.59	11.34	12.28	15.8
Fe ₂ O ₃	0.56	0.21	0.66	0.48	0.48	0.48	1.80	2.22	1.36	1.79	1.34	0.97	2.94	1.75	6.6
MnO	0.04	0.01	0.07	0.04	0.04	0.04	0.21	0.22	0.09	0.17	0.01	0.02	0.04	0.02	0.1
MgO	0.00	0.00	0.01	0.03	0.03	0.01	0.08	0.02	0.02	0.04	0.01	0.00	0.00	0.00	4.4
CaO	2.01	1.96	1.87	1.46	1.46	1.83	0.75	1.14	1.13	1.01	0.37	0.81	0.37	0.52	6.4
Na ₂ O	5.11	4.89	5.01	4.46	4.46	4.87	3.22	3.98	4.19	3.80	5.11	4.23	3.93	4.42	3.2
K ₂ O	2.12	2.43	1.69	4.21	4.21	2.61	4.71	3.59	4.25	4.18	3.18	4.09	3.53	3.60	1.9
P ₂ O ₅	0.00	0.00	0.00	0.00	0.00	0.00	0.01	0.00	0.01	0.01	0.00	0.01	0.00	0.00	0.2
LOI	0.32	0.35	0.27	0.31	0.31	0.31	0.41	0.24	0.65	0.43	0.72	0.84	0.31	0.62	
Total	99.44	99.56	99.59	99.72	99.72	99.58	99.79	99.46	99.46	99.57	99.46	99.41	99.83	99.57	98.4
Trace elements (ppm)															
Cs	0.54	0.56	0.66	0.54	0.54	0.58	0.41	0.52	0.43	0.45	0.19	0.29	0.21	0.23	
Rb	42.49	44.53	28.47	93.82	93.82	52.33	132.70	105.58	106.82	115.03	112.71	85.02	65.73	87.82	58.00
Ba	21.30	99.10	54.60	45.50	45.50	55.13	484.30	271.20	293.40	349.63	47.20	67.70	668.30	261.07	390.00
Sr	68.70	153.60	85.80	54.30	54.30	90.60	100.50	54.70	41.30	65.50	31.40	19.20	26.30	25.63	325.00
Pb	19.80	22.20	17.10	20.10	20.10	19.80	21.70	18.30	17.80	19.27	15.20	5.10	4.20	8.17	12.60
Th	1.06	0.18	2.23	1.64	1.64	1.28	18.08	11.04	6.78	11.97	2.83	3.49	7.48	4.60	5.60
U	2.22	0.23	3.18	1.48	1.48	1.78	8.55	12.13	5.64	8.77	10.64	2.38	1.93	4.98	1.42
Zr	20.70	5.80	151.28	31.16	31.16	52.24	713.55	614.40	470.78	599.58	1159	414.88	1189	920.92	123.00
Hf	0.40	0.20	5.30	1.60	1.60	1.88	17.80	14.10	9.90	13.93	38.20	10.50	25.60	24.77	3.70
Ta	0.35	0.29	0.36	0.17	0.17	0.29	0.69	0.68	0.53	0.63	16.08	0.94	1.76	6.26	1.10
Y	28.65	3.24	36.74	11.61	11.61	20.06	129.83	212.18	83.47	141.83	157.23	31.27	158.43	115.64	20.00
Nb	1.42	0.45	0.97	1.55	1.55	1.10	11.92	9.93	9.38	10.41	252.23	14.23	18.74	95.07	12.00
Sc	3.93	2.02	3.42	5.08	5.08	3.61		11.88	4.27	8.08	1.05	1.46	5.59	2.70	22.00
Co	86.12	102.06	51.16	40.31	40.31	69.91	36.10	45.02	54.42	45.18	79.80	102.13	71.37	84.43	
Ni	1.60	44.70	2.10	34.60	34.60	20.75	27.10	1.40	2.40	10.30	34.70	1.80	2.60	13.03	51.00
V	13.20	12.90	16.40	14.80	14.80	14.33	16.70	16.70	16.10	16.50	0.71	15.10	17.20	11.00	131.00
Ga	12.60	11.30	15.80	16.90	16.90	14.15	32.06	17.10	18.70	22.62	58.98	18.20	17.40	31.53	16.00
Zn	16.20	1.40	8.70	10.20	10.20	9.13	75.60	78.20	63.60	72.47	197.50	34.30	187.90	139.90	73.00
Cu	9.34	3.39	1.53	7.37	7.37	5.41	1.95	18.34	3.63	7.97	2.23	6.23	8.63	5.70	
Geochemical parameters and ratios															
A/CNK	1.07	1.07	1.09	1.05	1.05	1.07	1.14	1.11	1.04	1.10	1.03	0.98	1.04	1.02	
K ₂ O + Na ₂ O	7.23	7.32	6.70	8.67	8.67	7.48	7.93	7.57	8.44	7.98	8.29	8.32	7.46	8.02	5.10
K ₂ O/Na ₂ O	0.41	0.50	0.34	0.94	0.94	0.55	1.46	0.90	1.01	1.13	0.62	0.97	0.90	0.83	0.59

Table 4 (continued)

Rock type	Garnet-bearing trondhjemites				Garnet-rich syenogranites				Alkali feldspar granites				C.C ^a	
	Ad15	Ad25	Ad30	Ad39	Average	Ad29	Ad41	Ad46	Average	Ad.1	Ad10	Ad32		Average
CaO/Na ₂ O	0.39	0.40	0.37	0.33	0.37	0.23	0.29	0.27	0.26	0.07	0.19	0.09	0.12	2.00
Al ₂ O ₃ /TiO ₂	1.56	1.41	2.03	2.10	253.00	223.67	461.33	281.00	322.00	323.00	629.50	87.23	346.58	22.57
10,000*Ga/Al	414.19	453.01	492.78	372.51	433.13	294.65	282.27	330.29	302.40	313.03	399.35	445.83	386.07	252.00
K/Rb	0.59	0.24	0.31		0.38	1.32	1.82	2.54	1.89		4.47	2.38	2.40	0.18
Rb/Sr		2.23	1.92		2.07	3.65	2.57	2.75	3.04	0.42	0.80		0.61	6.72
Ba/Rb	1.99	0.45	0.52	2.06	1.26	0.27	0.39	0.36	0.34	2.39	1.26		1.82	0.15
Rb/Ba	29.92	98.96	29.35	60.53	47.68	11.13	10.63	11.39	11.05		5.97	3.51	4.74	4.83
Rb/Nb		1.55	2.69		2.77	17.28	14.60	17.70	16.53	15.69	15.14	10.65	13.82	10.90
Nb/Ta	4.06			7.49	7.35	10.89		8.90	9.90		2.20		1.22	1.71
Y/Nb		7.20	6.19	9.65	6.29	26.20	16.24	12.79	18.89		3.71	4.25	3.98	5.09
Th/Ta	3.03													
Rare earth elements (ppm)														
La	2.06	3.98	3.37	3.10	3.13	55.35	39.24	29.34	41.31	7.75	27.76	69.14	34.88	18.00
Ce	4.31	6.37	7.15	5.66	5.87	132.02	106.51	71.01	103.18	27.67	74.45	175.71	92.61	42.00
Pr	0.49	0.65	0.78	0.68	0.65	19.37	12.64	9.48	13.83	3.49	9.90	25.01	12.80	5.00
Nd	1.93	2.35	2.95	2.73	2.49	83.63	55.30	41.84	60.26	17.72	41.71	107.01	55.48	20.00
Sm	0.66	0.69	1.03	1.07	0.86	21.82	15.73	11.19	16.25	9.61	10.80	26.62	15.68	3.90
Eu	0.11	0.33	0.19	0.34	0.24	2.35	1.75	1.77	1.96	0.58	1.31	4.17	2.02	1.20
Gd	1.23	0.69	1.62	1.26	1.20	27.25	20.73	13.52	20.50	14.31	10.68	27.43	17.47	3.60
Tb	0.36	0.10	0.47	0.21	0.29	4.29	4.23	2.27	3.60	3.58	1.78	4.99	3.45	0.56
Dy	3.24	0.75	4.17	1.52	2.42	25.31	28.41	13.29	22.34	28.59	10.40	30.14	23.04	3.50
Ho	0.79	0.15	1.06	0.32	0.58	5.12	6.09	2.62	4.61	6.40	2.01	6.07	4.83	0.76
Er	2.67	0.46	3.68	0.99	1.95	15.34	18.67	7.80	13.94	22.49	5.83	18.11	15.48	2.20
Tm	0.43	0.06	0.61	0.14	0.31	2.28	2.75	1.16	2.06	3.78	0.82	2.59	2.40	
Yb	2.91	0.48	4.17	0.96	2.13	16.39	17.06	7.36	13.60	26.69	5.19	15.38	15.75	2.00
Lu	0.42	0.07	0.65	0.15	0.32	2.45	2.40	1.06	1.97	3.43	0.75	2.12	2.10	0.33
ΣLREE	9.56	14.37	15.47	13.58	13.25	314.54	231.17	164.63	236.78	66.82	165.93	407.66	213.47	90.10
ΣHREE	12.05	2.76	16.43	5.55	9.20	98.43	100.34	49.08	82.62	109.27	37.46	106.83	84.52	12.95
ΣREE	21.61	17.13	31.90	19.13	22.44	412.97	331.51	213.71	319.40	176.09	203.39	514.49	297.99	103.05
Eu/Eu*	0.37	1.44	0.45	0.89	0.79	0.29	0.30	0.44	0.34	0.15	0.37	0.47	0.33	0.96
(La/Yb) ^{N^a}	0.48		0.55	2.19	2.21	2.29	1.56	2.71	2.19		3.63	3.05	3.34	
(La/Sm) ^{N^a}	1.95	3.60	2.04	1.81	2.35	1.58	1.56	1.64	1.59	0.50	1.61	1.62	1.24	
(Gd/Lu) ^{N^a}	0.36	1.22	0.31	1.04	0.73	1.37	1.07	1.58	1.34	0.52	1.76	1.60	1.29	
(Ce/Yb) ^{N^a}	0.39		0.45	1.55	0.80	2.12	1.64	2.53	2.10		3.77	3.00	3.38	
(La/Lu) ^{N^a}	0.51	5.90	0.54	2.15	2.27	2.34	1.70	2.87	2.31	0.23	3.84	3.39	2.49	

Table 4 (continued)

Rock type	Garnet-bearing trondhjemites				Garnet-rich syenogranites				Alkali feldspar granites				C.C ^a
	Ad15	Ad25	Ad30	Ad39	Average	Ad29	Ad41	Ad46	Average	Ad.1	Ad10	Ad32	Average
(Gd/Yb) ^{N^a}	0.34	1.16	0.31	1.06	0.72	1.35	0.98	1.49	1.27	0.43	1.66	1.44	1.18
TE1–3	1.13	0.95	1.13	0.98	1.05	1.02	1.11	1.05	1.06	1.19	1.09	1.08	1.12
Quartz	36.07	36.81	40.21	30.88	35.99	39.06	37.66	32.85	36.52	34.14	35.72	41.46	37.11
Albite	49.57	46.91	48.39	41.66	46.63	30.15	38.25	39.31	35.90	45.90	38.37	36.00	40.09
Orthoclase	14.36	16.28	11.40	27.46	17.38	30.80	24.09	27.84	27.58	19.95	25.91	22.54	22.80
Corundum	0.95	0.96	1.23	0.66	0.95	1.69	1.37	0.53	1.20	0.40	0.00	0.41	0.27
TZr ^c C	656	808	808	682	715.39	956	946	889	930.33	988	873	1002	954.33
P	1.38	1.52	1.52	2.96	1.95	1.29	2.21	2.21	1.50	1.84	1.42	1.20	1.20
Depth (km)	3.70	4.10	4.10	7.99	5.27	3.48	5.97	5.97	4.05	4.97	3.83	3.24	3.24
log fO ₂	– 18.10	– 13.43	– 16.97	– 16.03	– 10.04	– 10.28	– 11.37	– 10.55	– 9.34	– 9.24	– 10.08	– 10.08	– 10.08

C.C^a average continental crust values (Rudnick and Fountain 1995); Fe₂O₃ as total iron; A/CNK is molar Al/(Ca+Na+K)
^aNormalized chondrite values from (Sun and McDonough 1989). The estimated depth based on the density of continental crust 2.7 g/cm³

Structure lineament map data extracted from the first PC of ASTER imagery data produced accurate structure trends in the Wadi El-Hima area (Fig. 5a, b). The main structure strike is NW–SE, which is parallel to the Najd fault system in the Central Eastern Desert of Egypt (Sultan et al. 1988), and other minor trends are NNE–SSW, N–S and E–W (Fig. 5a, b). A density lineament map indicates a highly dense set of structure pathways for hydrothermal solutions in trondhjemites and syenogranites that host garnets in the Wadi El-Hima area (Fig. 5c). These structure pathways share a NW–SE strike with the Najd fault system and are thus considered an ancient channel for magmatic-fluid flows, which drove metasomatism and formation of trondhjemites as well as facilitated residual garnet accumulation along the intrusive contact with alkali-feldspar granites (Figs. 2b–g, 3c–g, 5c). This is supported by field evidence showing a high concentration of garnet (up to 30 vol%) along intrusive contacts that strike NW–SE (Fig. 6c–f). Therefore, we suggest that magmatic-fluid flows along fault zones may play very important roles for collection and accumulation of residual garnets in partially melted garnet-rich granites along these zones.

As discussed previously, garnets in the Wadi El-Hima area are dominantly almandine in composition, and have high average concentrations of FeO (34 wt%) and Al₂O₃ (21 wt%), and minor amounts of MnO (4 wt%), and MgO (1.8 wt%) (Table 2; Supplementary 4). Ferric iron (Fe³⁺) has strong absorption characteristics at wavelengths of 1.3, 1.7, and 2.3 μ m, while Mn²⁺ has absorption characteristics near 0.41 μ m (Izawa et al. 2018). Because of FeO and Al₂O₃ enrichment in El-Hima garnets, ASTER sensor data in VNIR and SWIR bands can be used to detect and map these garnets. Consequently, remote sensing spectral mapping techniques (SAM and MF) provide reliable constraints on the locations of garnet accumulations and distribution in the Wadi El-Hima area (Fig. 6a–d). The accuracy of these techniques has been confirmed with fieldwork and lab analyses; so they represent an effective tool for economic mineral mapping in regions that may be inaccessible, and should encourage further future exploration of mineralized granites. Besides tracing garnet in host rocks, the results show other examples of garnet in Umm Asheira tonalites–granodiorites, pegmatite dykes in Gabal El-Faliq, and stream sediments (Fig. 6a–d). Tonalites–granodiorites in the eastern part of Wadi El-Hima are highly enriched in garnet (e.g., Umm Asheira) relative to those in the western part (Fig. 6c, d). False-colour composite images (7, 3, 1, in RGB) with decorrelation stretch enhancements allowed successful lithological discrimination of granitic phases with regards of garnet-bearing rocks in the Wadi El-Hima area (Fig. 6e).

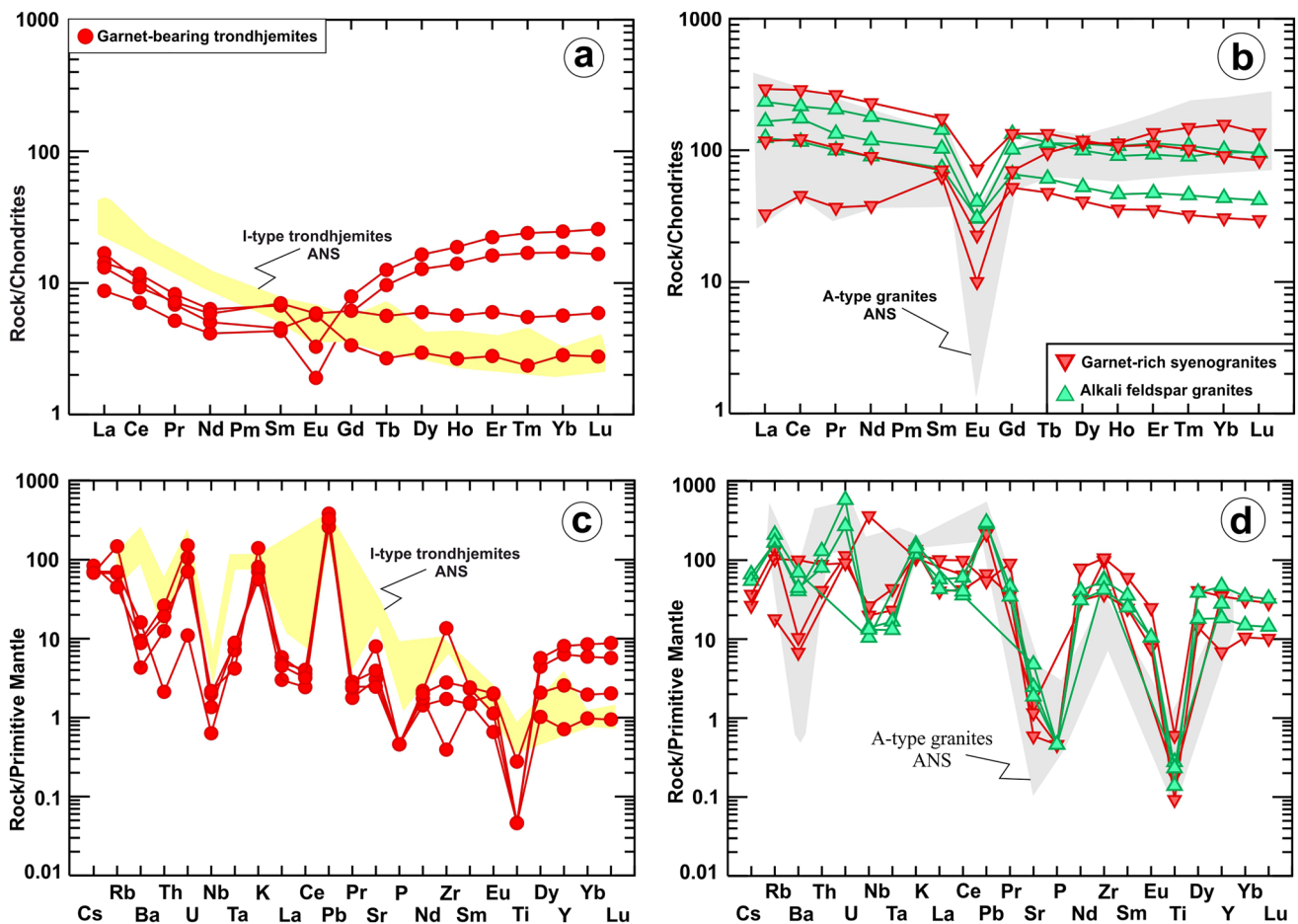


Fig. 9 Whole-rock chemistry of El-Hima mineralized granites. **a** Chondrite-normalized REE patterns of garnet-bearing trondhjemites. **b** Chondrite-normalized REE patterns of garnet-rich syenogranites and alkali feldspar granites. **c** Primitive mantle normalized trace elements of garnet-bearing trondhjemites. **d** Primitive mantle normalized trace elements of garnet-rich syenogranites and alkali feldspar

granites. Fields of ANS metasomatized I-type trondhjemites (Eliwa et al. 2014), and A-type granites (Sami et al. 2017) are used for comparison. REE and trace elements of granites were normalized to chondrite and primitive mantle values, respectively (Sun and McDonough 1989)

T, P and fO_2 conditions of granite crystallization

El-Hima garnet and subhedral ilmenite crystals (Supplementary 2d) were used to estimate a minimum temperature of garnet growth (Pownceby et al. 1987, 1991) using Mn partitioning in garnet-rich syenogranites and alkali-feldspar granites. This geothermometer produced values of 695 °C and 700 °C (Supplementary 4), respectively, suggesting that garnet equilibrated at the same conditions in both granite types. Equilibrium temperatures during cooling and crystallization can also be calculated by utilizing garnet-biotite Fe–Mg exchange thermometry (Bhattacharya et al. 1992; Holdaway 2000), where calculated temperatures of equilibration (T_{GB}) range from 680 °C–730 °C for garnet-rich syenogranites (Supplementary 4). Consequently, estimated temperatures of formation of Wadi El-Hima garnets lie within the range ~680 to 730 °C, which straddles the wet

solidus for granitic and intermediate magmas in the middle to upper continental crust (Palin et al. 2016).

Zircon saturation temperatures (T_{Zr}) were calculated based on the whole-rock chemistry of granites using the parameterization of Watson and Harrison (1983). Zircon crystallizes early from granitic magmas and its partition behavior is mainly controlled by temperature. Slightly elevated Zr contents in alkali feldspar granites (Zr: 415–1189 ppm) and garnet-rich syenogranites (Zr: 471–714 ppm) compared to garnet-bearing trondhjemites (Zr: 4–151 ppm) suggest derivation of the former from melts of significantly high temperatures (Watson and Harrison 1983; El-Bialy and Omar 2015; Sami et al. 2020), assuming zirconium saturation in the melt. Therefore, T_{Zr} averages 955 °C, 930 °C, and 715 °C for alkali feldspar granites, garnet-rich syenogranites and garnet-bearing trondhjemites, respectively (Table 4). These temperatures of El-Hima

A-type granites (935 °C on average) resemble those of the northern ANS A-type granites from Wadi Al-Baroud (El-Bialy and Omar 2015). Calculated results for the studied El-Hima garnets (680–730 °C) represent minimum temperatures at which garnet crystallized from the host magmas, but zircon saturation temperatures (715–955 °C) represent a maximum temperature limit. These conditions are similar to magmatic garnets with lower temperatures of formation (590–645 °C) than their host granites (733 ± 28 °C), such as the Abu Diab A-type granites in the Central Eastern Desert of Egypt (Sami et al. 2020 and reference therein).

Garnet geobarometry estimated from coexisting garnet and biotite (Wu 2019) in garnet-rich syenogranites is 2.93 kbar and in alkali feldspar granites is 2.1 kbar (Supplementary 4), reflecting formation of host granites in the upper crust. This is consistent with magmatic garnets (~1 vol%) in Madha granodiorites from ANS (du Bray 1988) and garnet-bearing muscovite granites in Abu Diab area (Sami et al. 2020) that are late-stage crystallization products of peraluminous magmas that cooled at low pressures (<3 kbar). Based on whole-rock chemistry (Table 4), a numerical method can be used to estimate crystallization pressure of granitic intrusions based on two polynomial equations (Yang 2017): (1) $P = -0.2426 \times (\text{Qtz})^3 + 26.392 \times (\text{Qtz})^2 - 980.74 \times (\text{Qtz}) + 12,563$, where Qtz is the normative quartz and P is pressure in megapascal (MPa). (2) $P = 0.2426 \times (\text{Ab} + \text{Or})^3 - 64.397 \times (\text{Ab} + \text{Or})^2 + 2981.3 \times (\text{Ab} + \text{Or}) - 464,224$, where P is pressure in MPa, and the sum of the CIPW norm (Qtz + Ab + Or) contents is 100%. The calculated pressure (Table 4) of garnet-bearing trondhjemites using these polynomial equations ranges from 1.20 to 2.96 kbar. This is consistent with experimental results showing that garnet stable in silicic liquids at low pressures (~3 kbar) have spessartine contents up to 10 mol% (Green 1977), similar to our garnet spessartine (33.3–15 mol.%; Supplementary 4). Assuming a typical lithostatic pressure gradient of 1 kbar \approx 3.3 km overburden, these data imply crystallization depths of less than 10 km below the Earth's surface. The garnet-rich syenogranites yielded variable pressures from 1.3 to 2.2 kbar, equating to depths less than ~7 km, whereas alkali feldspar granites crystallized at low pressure (1.42–1.84 kbar) and very shallow depth (<5.5 km). Additionally, the Qz–Ab–Or diagram of normative compositions (Fig. 11d) shows that Wadi El-Hima granites lie close to the minimum melt composition at ~2 kbar to ~4 kbar with excess H₂O fluid containing 0.5–1% F (Manning 1981). Increasing water pressure shifts the position of the granite minimum melting curve towards albite-rich compositions, supporting the importance of hydrothermal fluids during the metasomatic origin of garnet-bearing trondhjemites as opposed to a magmatic origin for garnet-rich syenogranites and alkali feldspar granites.

The oxygen fugacity ($f\text{O}_2$) of the Wadi El-Hima granites was also calculated from the equilibrium expression equation [$\log f\text{O}_2 = -30,930/T + 14.98 + 0.142(P - 1)/T$; Wones 1989], where T is temperature (in Kelvin), and P is pressure (bars). Using the previously constrained pressure and temperature (T_{Zr}) conditions of crystallization, the calculated oxygen fugacity ($\log f\text{O}_2$) of garnet-bearing trondhjemites ranges from –13.43 to –18.1. In addition, garnet-rich syenogranites have $\log f\text{O}_2$ values in the range –10 to –11.4 and alkali feldspar granites yield –9.3 to –11.8 (Table 4), indicating that the Wadi El-Hima granites were strongly oxidized (Helmy et al. 2004 and references therein). Using a T – $f\text{O}_2$ diagram (Supplementary 5b), the Wadi El-Hima granites plot in the field of titanite + magnetite + quartz, within the range from –9.5 to –18, suggesting that they were derived from a hydrous and oxidized source (Wones 1989).

Petrogenesis of Wadi El-Hima granites

Magma type and tectonic setting

All types of El-Hima granites are peraluminous in compositions (Fig. 10a) (Maniar and Piccoli 1989). Garnet-bearing trondhjemites show characteristics of highly fractionated peraluminous I-type granites ($\text{A/CNK} = 1.05$ – 1.09) with high Al_2O_3 (15.1 wt%, on average) and SiO_2 (74.4 wt%), but low $\text{K}_2\text{O}/\text{Na}_2\text{O}$ (0.55), ΣREE (22.4 ppm), Zr (51.5 ppm), Y (20.1 ppm), Nb (1.1 ppm) and Th (0.90 ppm) (Fig. 10a, c; Table 4) (Chappell and White 1992). Moreover, chondrite-normalized REE patterns (Fig. 9a) of El-Hima garnet-bearing trondhjemites are similar to those of ANS I-type trondhjemites that formed in a volcanic arc setting (Eliwa et al. 2014).

Wadi El-Hima garnet-rich syenogranites and alkali feldspar granites are weakly to strongly peraluminous with A/CNK ratios (>1) and high $10^4 \times \text{Ga}/\text{Al}$ values (2.3–8.6) (Fig. 10a; Table 4). They also have high ΣREE (308 ppm on average), high LILE (e.g., Rb, Cs, K; Table 4) and high HFSE (e.g., Zr, Ta and Nb). Therefore, these granites show an affinity to A-type granites (Fig. 10b), rather than fractionated I-type and S-type granites (e.g., Whalen et al. 1987; Eby 1992; Frost et al. 2001; El-Bialy and Omar 2015; Sami et al. 2020). This is supported by their position on a Zr vs. $10^4 \times \text{Ga}/\text{Al}$ diagram (Whalen et al. 1987), where garnet-rich syenogranites and alkali feldspar granites plot in the A-type granite field, but garnet-bearing trondhjemites lie in the I and S-type granite fields (Fig. 10c). A-type granites are classified into: A1 granites, which form in an intraplate tectonic setting and have a mantle affinity, and A2 granites, which form in a post-collisional setting and have a crustal signature (Eby 1992). The investigated granites have an A2-type affinity, except for one sample of alkali feldspar

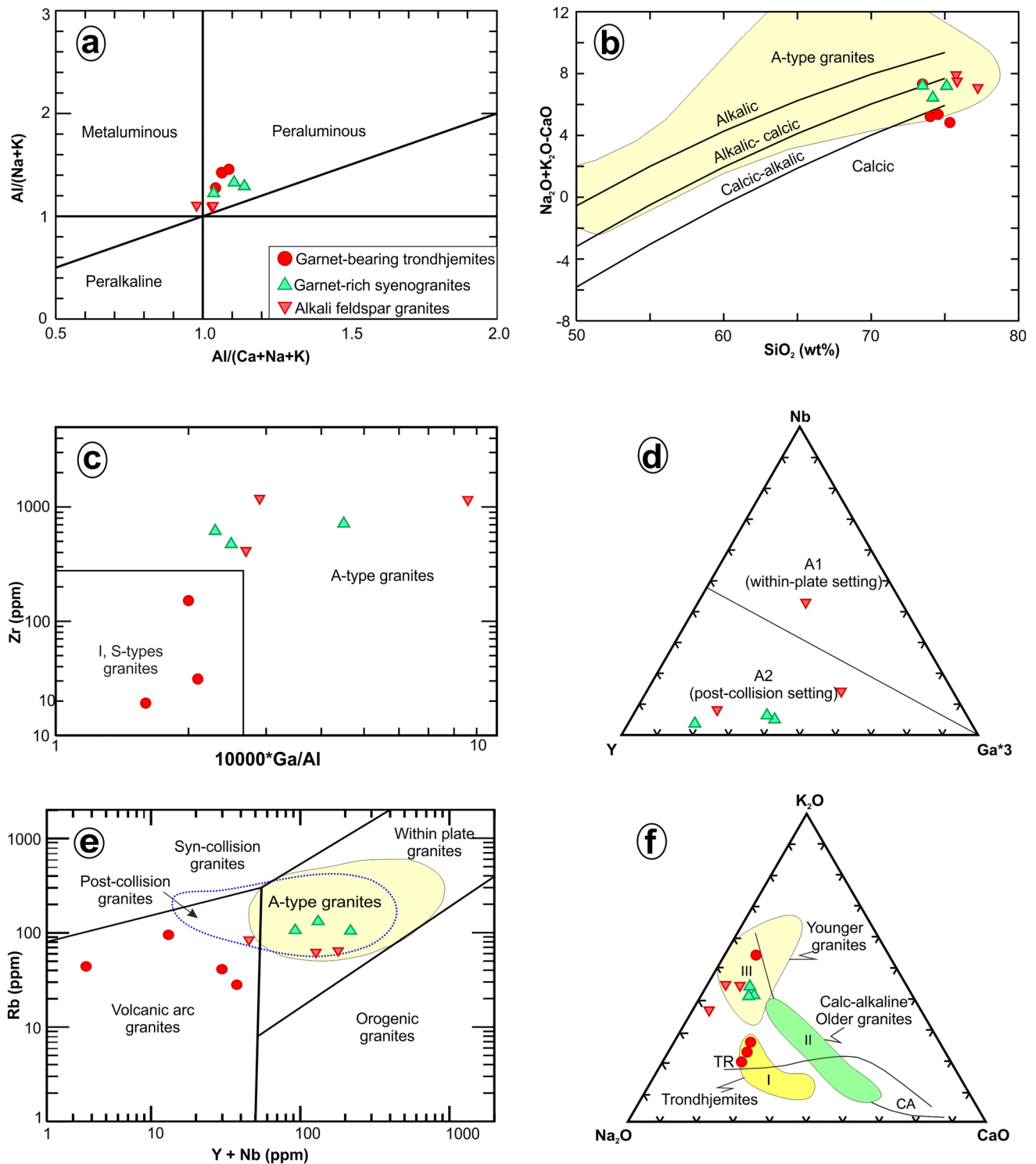


Fig. 10 Whole-rock major oxides of Wadi El-Hima granites. **a** Molar $Al_2O_3/(Na_2O+K_2O)$ versus $Al_2O_3/(CaO+Na_2O+K_2O)$ for Wadi El-Hima granites (Maniar and Piccoli 1989). A-type granite field is after Whalen et al. (1987). **b** Chemical classification diagram using SiO_2 versus $(Na_2O+K_2O)-CaO$ (Frost et al. 2001). **c** $10^4 \times Ga/Al$ against Zr for distinguishing between I, S, M and A-type granites

(Whalen et al. 1987). **d** Nb-Y-Ga/3 discrimination diagram for sub-division of A-type granites into A1 and A2 sub-types (Eby 1992). **e** Y+Nb vs. Rb tectonic discrimination diagram (Pearce et al. 1984). **f** Na_2O-K_2O-CaO ternary diagram of Egyptian granitoids (Hassan and Hashad 1990; Sami et al. 2017). Trondhjemites and calc-alkaline fields are after Barker and Arth (1976)

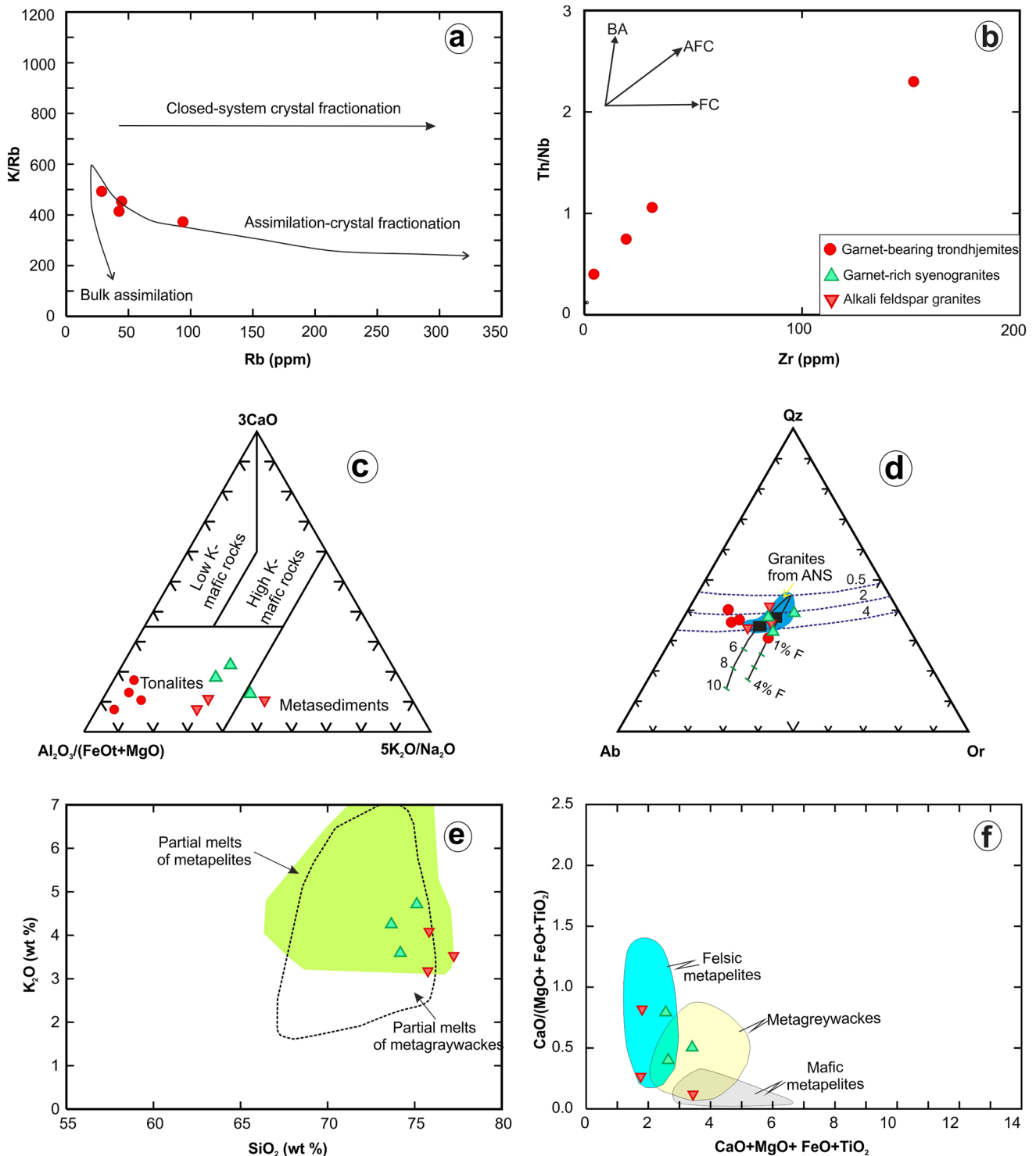


Fig. 11 Model for the origin and thermometry of Wadi El-Hima granites. **a** Rb versus K/Rb diagram (Akinin et al. 2009). **b** Zr vs. Th/Nb variation diagrams of Wadi El-Hima I-type granites, showing fractional crystallization (FC), assimilation-fractional crystallization (AFC), and bulk assimilation (BA) trends (Nicolae and Saccani 2003). **c** Petrogenetic discrimination $\text{Al}_2\text{O}_3/(\text{FeOt} + \text{MgO}) - 3\text{CaO} - 5(\text{K}_2\text{O}/\text{Na}_2\text{O})$ ternary diagram (Laurent et al. 2014) for Wadi El-Hima I- and A-type granites. **d** Normative composition of Qz–Ab–Or projection for granite thermometry. Dashed lines show quartz-alkali feld-

spar cotectics and trace of water saturated minimum melt compositions at total pressure ranging from 0.5 to 10 kbar (Holtz et al. 1992). Solid line shows trace of minimum melt compositions at 1 kbar with excess H_2O and increasing fluorine (F, up to 4 wt%) (Manning 1981). **e**, **f** Composition of Wadi El-Hima A-type granites compared to melts produced by experimental dehydration melting of metasedimentary rocks. Fields of melt compositions in panel **e** is after Patino Douce (1999) and in panel **f** is after Gerdes et al. (2000)

granite from Gabal El-Faliq, which resembles an A1-type granites (Fig. 10d). This is consistent with other studies of A-type granites in the Eastern Desert, which are considered as A2-type granites and have been ascribed to formation in a post-collisional setting (e.g., Sami et al. 2017; Azer et al. 2019; Seddik et al. 2020). Finally, Wadi El-Hima A-type granites exhibit nearly flat REE patterns (Fig. 9b), similar to those of Egyptian A-type granites (Sami et al. 2017), except garnet-rich samples that are enriched in HREE relative to LREE. They are poor in Ba, Sr, Ti and P due to fractionation of plagioclase and apatite during formation of early formed I-type granites (Fig. 9d; Table 4).

Garnet-rich syenogranites and alkali feldspar granites show alkali to calcic-alkalic characteristics and plot in the field of A-type granites on discrimination diagrams (Frost et al. 2001) (Fig. 10b); however, garnet-bearing trondhjemites have calcic characteristics, reflecting an abundance of plagioclase and a relative depletion of potash feldspars (Fig. 10b). On a tectonic discrimination diagram of Rb vs. Y + Nb (Pearce et al. 1984), the Wadi El-Hima A-type garnet-rich syenogranites and alkali feldspar granites appear to be post-collision granites (Fig. 10e). By contrast, garnet-bearing trondhjemites lie in the field of volcanic arc granites (Fig. 10e), and are considered as collision-related granites. They are rich in LILE relative to HFSE, and show a strong positive spike of Pb (Fig. 9c), reflecting a subduction-related continental arc setting (Eliwa et al. 2014). In summary, Wadi El-Hima I-type garnet-bearing trondhjemites crystallized from peraluminous magmas in a volcanic-arc tectonic setting during arc-arc collision, while both A-type garnet-rich syenogranites and alkali feldspar granites originated in a post-collision setting (Fig. 12).

Model for the origin and geodynamic evolution of the Wadi El-Hima granites

Mantle materials have very low Rb/Sr ratios ($Rb/Sr < 0.1$; Taylor and McLennan 1985), while lower, middle and upper continental crust have Rb/Sr ratios of 0.12, 0.22 and 0.32, respectively (Rudnick and Fountain 1995). The average values of Rb/Sr ratio of Wadi El-Hima I-type and A-type granites are 0.38 and 2.51, respectively (Table 4), similar to that of the continental crustal materials that were involved in generating the El-Hima granites. Mantle-derived rocks have higher Nb/Ta values (> 17.5) than continental crustal materials ($Nb/Ta > 17.5$) (Rudnick and Fountain 1995; Taylor and McLennan 1985; Green 1995). The average Nb/Ta values of Wadi El-Hima I-type (2.77) and A-type granites (15.17) are consistent with crystallization from crustal-sourced magmas. Mantle sources have a lower Y/Nb ratio (< 1.2) than crustal sources ($Y/Nb > 1.2$; Eby 1992). The Wadi El-Hima I-type and A-type granites have high Y/Nb ratios of 7.35 and

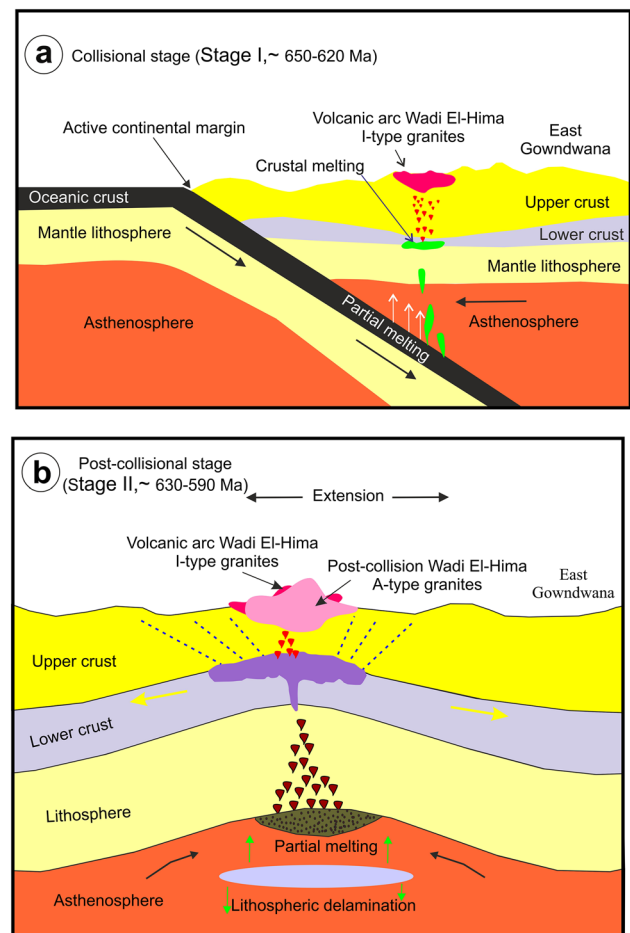


Fig. 12 Simplified model for the tectonomagmatic evolution of the juvenile crust in the Wadi El-Hima granites in the Eastern Desert of Egypt. **a** First stage of I-type granite formation at an active continental margin. **b** Second stage of A-type granite formation during the post-collisional stage. This stage shows lithospheric delamination, partial melting of lower crust and the generation of A-type granites in the upper crust (modified after Azer et al. 2019). The crust and mantle thickness are not to scale

9.9, respectively, suggesting their parental magmas formed from melting of crustal rocks (Table 4). In addition, mantle derived magmas have a lower K/Rb (~ 100 ; Akinin et al. 2009) ratio than lower continental crust ($K/Rb = 413$), middle crust ($K/Rb = 270$) and upper crust ($K/Rb = 250$; Rudnick and Fountain 1995). Wadi El-Hima I-type and A-type granites have a high K/Rb ratio of 433 and 344, respectively, reflecting their parental magmas having been derived from melting of lower crustal rocks.

Some diagnostic major oxides and trace element ratios of Wadi El-Hima I-type granites (Fig. 11a, b) have been used to infer their petrogenesis and magmatic processes, such as bulk assimilation, assimilation–fractional crystallization (AFC) and fractional crystallization (FC) (De Paolo 1981). Based on a Rb versus K/Rb diagram (Akinin et al. 2009) and

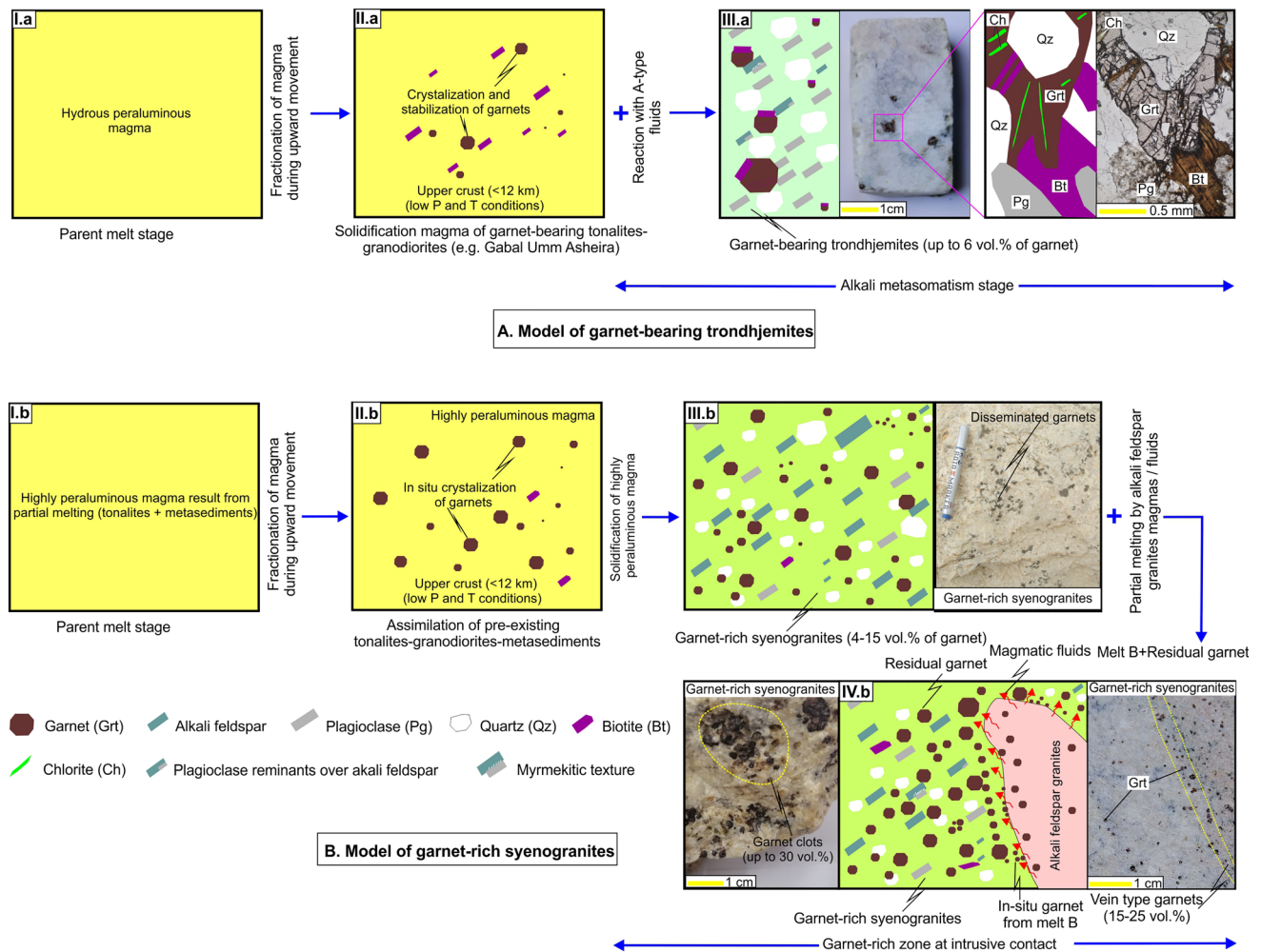


Fig. 13 Sketch showing genesis of garnets in Wadi El-Hima granites. **a** Model for garnet-bearing trondhjemites. **b** Model for garnet-rich syenogranites. Garnets crystallized from hydrous peraluminous

granitic magmas in the late stage in the upper crust. Alkali feldspar granitic magmas assimilate syenogranites along the intrusive contact zone to form melt B + residual garnets

Th/Nb ratios versus Zr contents (Nicolae and Saccani 2003), Wadi El-Hima I-type granites show clear assimilation and fractional crystallization trends (Fig. 11a, b). The investigated granites also exhibit distinct negative Nb anomalies (Fig. 9d; Table 4), indicating involvement of crustal materials and crustal contamination (Nicolae and Saccani 2003). Therefore, the most suitable differentiation mechanism in this case is AFC (Fig. 11a, b). Throughout this process, lower crustal rocks (e.g., tonalites-metasediments; Fig. 11c) could also partially melt during lithospheric delamination (Fig. 12b). The resultant melts would fractionate during ascent and so crystallize in the upper crust to produce Umm Asheira tonalites and granodiorites (Fig. 1c), where some of these tonalites (Fig. 12c) may then be metasomatized to produce El-Hima garnet-bearing trondhjemites. We observed textural and chemical evidence supporting a metasomatic origin of garnet-bearing trondhjemites, including: (1) replacement of oligoclase by K-feldspar and widespread

formation of perthitic and myrmekitic textures (Fig. 3c; Supplementary 2a); (2) primary biotite being partially or completely replaced by chlorite (Fig. 3a); (3) REE and spider diagrams of garnet-bearing trondhjemites (Fig. 9a, c) resemble those of ANS metasomatized trondhjemites (Eliwa et al. 2014); (4) calculated pressure (1.4–3.0 kbar) and temperature (656–808 °C) conditions (Table 4) of El-Hima trondhjemites are similar to those of ANS I-type tonalites (692–775 °C) (El-Bialy and Omar 2015), suggesting a metasomatic origin after tonalites; (5) the El-Hima trondhjemites show lower temperatures (656–808 °C; Table 4) than associated magmatic A-type granites (930–954 °C), reflecting a metasomatic origin after the parent tonalite-granodiorite bodies that have been affected by A-type magmatic fluids (Fig. 13a). This evolution is similar to the Rockford granites from the Appalachians, which were transformed to trondhjemites by alkali metasomatism caused by infiltration of Na-rich fluids (Drummond et al. 1986).

A-type granites in the Eastern Desert and Sinai have evolved in a transitional post-collisional setting from compression to extension by melting of crustal rocks during lithospheric delamination and slab breakoff (e.g., Moghazi et al. 2004; Eyal et al. 2010; El-Bialy and Omar 2015; Azer et al. 2019). Wadi El-Hima A-type granites are strongly peraluminous (A/CNK : 1.04–1.14; Table 4; Fig. 10a) due to a high proportion of crustal rocks in the source region for magma generation (Moghazi et al. 2004; Eyal et al. 2010; El-Bialy and Omar 2015). They are enriched in total alkalis, Rb, Pb, Th and have total REE (309 ppm), but are depleted in Nb, P, Ti, Sr and have a negative Eu anomaly (Table 4; Fig. 9b, d), also suggesting their derivation from a crustal source (Fig. 11c) coupled with advanced degrees of differentiation (Fig. 11a, b) in a post-collisional setting (Fig. 10e). El-Hima A-type granites lie in the field of tonalites-metasediments (Fig. 11c, e, f) based on parental source diagrams (Laurent et al. 2014; Patino Douce 1999; Gerdes et al. 2000). This suggests that tonalites-metasediments could provide a suitable protolith for Wadi El-Hima A-type granites. This is in agreement with the origin of A-type granitic magmas in Egypt after partial melting of a tonalitic to granodioritic source, which formed during the island-arc collisional stage (Farahat et al. 2007; Eyal et al. 2010). Pelite-derived melts in post-collisional settings are strongly peraluminous and may crystallize granites, similar to the Wadi El-Hima A-type granites (Fig. 11e, f). Therefore, we suggest that Al-rich crustal rocks (e.g., tonalites and metasediments) may be sources of the Wadi El-Hima peraluminous A-type granite enriched in garnets. This assumption agrees with tonalite and metasediment being sources for some A-type granites in ANS (Moghazi et al. 2004; Farahat et al. 2007; El-Bialy and Omar 2015; Sami et al. 2017).

Figure 12 shows a geodynamic model for the origin of El-Hima mineralized granites. The collisional stage between intraoceanic arc systems or accretion of a volcanic arc system onto the margin of East Gondwana occurred during the evolution of Neoproterozoic juvenile ANS crust. The first collisional stage (Stage I, ~650–620 Ma after Kröner et al. 1994; Stern 1994) (Figs. 10c, e, 12a) of Wadi El-Hima was associated with the origin of arc-related calc-alkaline I-type tonalites–granodiorites (Figs. 1c, 12a), which crystallized from magmas derived from assimilation of lower crustal rocks (e.g., tonalites-metasediments) by FC processes (Fig. 11) (Miller et al. 2001; Eliwa et al. 2014; El-Bialy and Omar 2015; Azer et al. 2019). During ascent of these peraluminous magmas, the magmas experienced fractional crystallization to produce the Umm Asheira tonalites–granodiorites (Fig. 1b, c) (protoliths of the Wadi El-Hima trondhjemite; Fig. 11c) with appreciable volumes of garnet (Figs. 2, 6, 13). Thus, garnets in El-Hima trondhjemites compositionally resemble garnets in Umm Asheira tonalites–granodiorites (Supplementary 6c). Spectral remote sensing signatures

(SAM and MF) show high concentration of almandine-rich garnets in tonalites–granodiorites in Gabal Umm Asheira in the east of the Wadi El-Hima region (Fig. 6c, d), similar to garnet signatures in Wadi El-Hima mineralized granites (Fig. 6c, d). El-Hima trondhjemites have similar garnet contents to Sikait garnet-rich granites (4 vol% garnet) that occur close to the El-Hima area (Moghazi et al. 2004) and the garnet-rich (up to 10 vol%) tonalites in NE Iran (Plimer and Moazzez-Lesco 1980). In addition, our field observations indicate that El-Hima I-type trondhjemites and syenogranites (Fig. 1b, c) are intruded by A-type alkali feldspar granites. Consequently, we suggest that post-collision A-type granitoids intruded into arc collision I-type trondhjemites (Fig. 10e).

During the post-collisional stage (Stage II, 630–590 Ma after Johnson et al. 2011) (Figs. 10e, f, 12b), lithospheric delamination and crustal thickening during low-angle subduction were followed by a slab break-off event (Schott and Schmeling 1998; Li et al. 2016) associated with a high thermal anomaly, which caused partial melting of pre-existing tonalites and metasediments in the lower crust (Fig. 11c–f). The high degree of partial melting was likely driven by upwelling of hot asthenosphere during lithospheric delamination (Avigad and Gvirtzman 2009). The resultant magmas ($T=954\text{ }^{\circ}\text{C}$) may have assimilated rims of pre-existing tonalites–granodiorites (e.g. Umm Asheira), and become highly peraluminous before crystallizing in the upper crust (Fig. 12a) forming: syenogranites rich in garnets (~4–10 vol%; Figs. 2d–g, 3d–g, 6f, 13b) around pocket of tonalites–granodiorites (i.e. the protoliths of trondhjemite). These syenogranites (Fig. 1c) formed from highly peraluminous magmas at the beginning of the post-collisional stage of the ANS (Fig. 12b). The more felsic magma residues ($\text{SiO}_2 \geq 76\text{ wt\%}$; Table 4) were associated with voluminous magmatic fluids produced by fractionation of peraluminous magmas. These formed after garnet-rich syenogranites, and may have crystallized alkali feldspar granites in the late post-collisional stage. Therefore, alkali feldspar granites intruded into syenogranites and post-date them (Figs. 2a, b, 12b). These felsic A-type magmas not only crystallized alkali feldspar granites, but also converted pocket of tonalites–granodiorites within syenogranites by magmatic fluids to produce metasomatized garnet-bearing trondhjemites (Figs. 11c, 13a). The trondhjemites occur as pockets inside El-Hima syenogranites (Fig. 1c), and contain up to ~6 vol% garnet (Figs. 2c, 3a, b, 13a). In addition, the orthoclase contents of K-feldspar in these trondhjemites (Or_{85-97}) and alkali feldspar granites (Or_{91-98}) are higher than those of garnet-rich syenogranites (Or_{76-88}), implying K-metasomatism of trondhjemites is related to alkali feldspar granitic magmas rather than syenogranites (Table 1; Supplementary 4). Finally, El-Hima A-type garnet-rich syenogranites and alkali feldspar granites formed during the post-collisional stage during the

evolution of the ANS (Fig. 12b) (e.g., Sami et al. 2017; Azer et al. 2019). This is also confirmed from the NW–SE striking Najd fault (620–540 Ma; Robinson et al. 2017) that crosscuts the Wadi El-Hima trondhjemites, syenogranites and alkali feldspar granites (Figs. 1c, 5a).

Shearing and extensional stress during the post-collisional period of an orogeny may enable fault planes to propagate to greater depths in the crust and open fault-defined shear zones (Azer et al. 2019; Seddik et al. 2020), such as the NW–SE Najd fault (Fig. 1c, 5a). These shear zones and faults provided a suitable channel for allowing mantle-derived melts and magmatic fluids to ascend through the crust and conduct heat to shallower crustal levels, enhancing partial melting of pre-existing tonalites and granodiorites (Fig. 12b). The remote sensing lineament density map for our study region (Fig. 5c) clearly shows structural pathways of magmatic/hydrothermal fluids penetrating NW–SE along the Najd fault system. The Najd fault system characterizes the final stages of east and west Gondwana assembly through a complex history of convergence, magmatism, and terrane exhumation in the ANS (e.g., Meyer et al. 2014). Some syenogranites suffered partial melting and alkali metasomatism (Figs. 2a, b, d, 3c) along intrusive contacts with the NW–SE striking Najd fault system (Figs. 1c, 6e) during this event, forming accumulations of residual garnet (Fig. 13b).

Genesis of garnets

There are several mechanisms that can explain garnet formation in granitic rocks. These include: (1) restitic garnet reacting with fluids/melts to form secondary biotite at its rims, although its core retains a magmatic origin (e.g., Rene and Stelling 2007); (2) peritectic garnet formed from dehydration melting of biotite in country rocks during ascent/emplacement of magma and is rich in inclusions (e.g., biotite, apatite, sillimanite, and zircon) and HREE, Sc, and Zr and poor in Zn, P, and U (e.g., Taylor and Stevens 2010; Dorais and Tubrett 2012; Dorais and Campbell 2022); (3) xenocrystic garnet derived from partially assimilated metamorphic rocks (e.g., Erdmann et al. 2009); (4) secondary metasomatic garnet formed during the interaction between post-magmatic hydrothermal fluids and the hosting granites, leading to post-magmatic growth of garnet (e.g., Kontak and Corey 1988; Clarke and Rottura 1994); (5) garnet phenocrysts crystallized directly from a melt at high pressures in the lower crust, and may be transported to higher crustal levels during magma ascent (e.g., Harangi et al. 2001); (6) magmatic garnet crystals precipitated from differentiated Mn-enriched peraluminous magmas at low-to-moderate pressures (e.g., Miller and Stoddard 1981; du Bray 1988; Sami et al. 2020); (7) magmatic garnets with high FeO contents (> 30 wt%) crystallized directly in strongly

peraluminous S-type granites, dacites or rhyolites at low-pressures in the upper crust (e.g., Clemens and Wall 1981).

The Wadi El-Hima garnets have high almandine contents (65–91 mol%) with subordinate pyrope (1.3–16.2 mol%), spessartine (3.3–15 mol%) and grossular (2.5–15 mol%) contents (Table 2; Supplementary 4), and also show low equilibrium temperatures (680–730 °C; Supplementary 4) and pressures (2.1–2.9 kbar; Supplementary 4). The Wadi El-Hima garnets differ in chemistry and texture (Figs. 3, 7, 14; Table 2) from xenocrystic garnets (e.g., Dorais and Tubrett 2012), garnet phenocrysts formed at high pressure (> 7 kbar) (Green and Ringwood 1968; Harangi et al. 2001) and peritectic garnets (Dorais and Tubrett 2012). Peritectic garnets that form due to reaction of biotite with fluids/melts often have several small inclusions (e.g., biotite) and high pyrope contents (27–30 mol%), in contrast with El-Hima homogenous garnets (Fig. 3c–g, 14c, Supplementary 1a, b). This rules out these mechanisms as being responsible for formation of the studied examples.

Magmatic and hydrothermal garnet in granites can sometimes be difficult to identify. Metasomatic garnets show similar compositions to magmatic garnets, but both types generally differ in terms of textures and other silicate mineral chemistry (Kontak and Corey 1988). Hydrothermal garnets are associated with secondary minerals (i.e. metasomatized types) and generally accumulate in open fracture and fissure spaces, forming veins-type ores, ore reticulates, and patches (Kontak and Corey 1988). For instance, they are often associated with metasomatized plagioclase (An_{0-7}) and secondary biotite and muscovite, which is not the case for the El-Hima examples (Table 1, Supplementary 4), ruling out a hydrothermal origin for the studied garnets.

Garnets in Wadi El-Hima trondhjemites are generally homogenous, large to medium, and anhedral to ridge-shaped crystals that are rimmed and dissected by biotite (Fig. 3a, b), similar to restite garnets (Rene and Stelling 2007). The occurrence of biotite rims and crosscutting veins in trondhjemite garnet indicates that the biotite grew due to garnet breakdown, likely via the following reaction: $liquid_1 + garnet = biotite + liquid_2$ (Rene and Stelling 2007), suggesting that they are restitic in nature (Fig. 3a, b). This biotite may thus be interpreted as the product of a garnet-consuming hydration reaction during cooling and decreasing pressure as a granitic melt rose in the crust. The restite garnets in garnet-bearing granites from the Trebic pluton (Rene and Stelling 2007) are magmatic in origin, but their rims decomposed to form biotite; they contain significant amounts of pyrope (7–17 mol%), similar to El-Hima garnets (6–16 mol%) in I-type granites (Fig. 14, Table 2, Supplementary 4). Thus, garnets in trondhjemites have affinity to restitic grains, and also overlap in compositional space with magmatic garnet (Fig. 14). These restite garnets have higher pyrope (6–16 mol%) and grossular (2–15 mol%) contents but lower

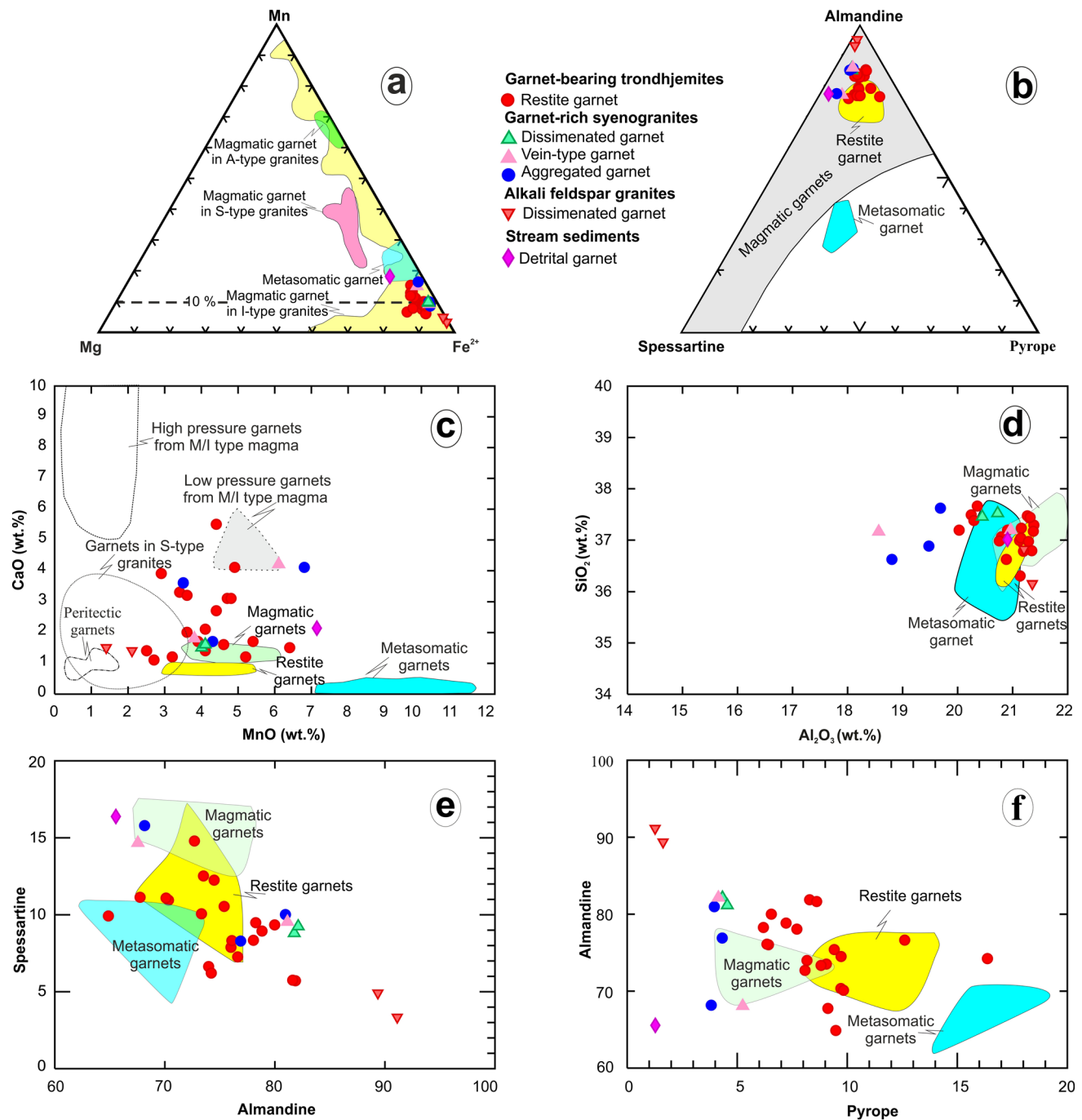


Fig. 14 Chemical compositions of Wadi El-Hima garnets. **a** Mg-Mn-Fe²⁺ ternary diagram for garnets in El-Hima I- and A-type granites and stream sediments compared with magmatic garnets in various granitic and metapelitic rocks (Harangi et al. 2001; Samadi et al. 2014). Magmatic garnets in highly fractionated A-type granites (Sami et al. 2020; Seddik et al. 2020), magmatic garnets in peraluminous S-type granites and pegmatites (du Bray 1988; Dahlquist et al. 2007; Gharib 2012), magmatic garnets in I-type granites (Miller and Stoddard 1981) and metasomatic garnets (Kontak and Corey 1988) are used for comparison. **b** Ternary diagram of spessartine-almandine-

pyrope showing magmatic (Clarke 1981) and metasomatic garnet fields (Kontak and Corey 1988). **c** CaO versus MnO (wt%) diagram (modified after Harangi et al. 2001; Samadi et al. 2014; Qin et al. 2021). **d** Al₂O₃ versus SiO₂. **e** Almandine versus spessartine **f** Almandine versus pyrope binary diagrams. High pressure (Harangi et al. 2001 and reference therein), peritectic (Taylor and Stevens 2010; Dorais and Tubrett 2012), metasomatic (Kontak and Corey 1988), magmatic garnets (Moghazi et al. 2004; Rene and Stelling 2007; Emam et al. 2011) and restite garnets (Rene and Stelling 2007) are shown for comparison

andradite (0–3 mol%) contents than garnets in syenogranites (Supplementaries 4, 6c), caused by the growth of biotite in their rims and possibly metasomatic modification during late magmatic or post-magmatic evolution.

Based on field investigation (Fig. 2d–h) and petrography (Fig. 3c–g; Supplementary 2b–d), the Wadi El-Hima syenogranites preserve three garnet occurrences: disseminated subhedral to rounded crystals, vein type and grain aggregates or clots (Figs. 3, 13; Supplementary 2). The vein-type (Fig. 2e) and aggregated garnets (Fig. 2f, g) are accumulation of subhedral to rounded disseminated grains. There is no difference in texture (i.e. they are homogenous and free of inclusions; Fig. 3e) or chemistry (Supplementaries 4, 6c; Fig. 14) between all three garnet occurrences. Garnets in syenogranites and alkali feldspar granites have very similar chemical compositions (Table 2; Supplementary 4) and plot mainly in the magmatic garnet field (Figs. 7, 14). They likely crystallize directly from the same Al-rich hydrous magma source (e.g., Hogan 1996; Dahlquist et al. 2007), which had a high FeO content (e.g., Clemens and Wall 1981; Rene and Stelling 2007), during the late stage of upper crustal magmatism, but accumulated by different mechanisms (Fig. 13). Other evidences for the garnets in the Wadi El-Hima A-type granites having a magmatic origin are summarized as follows: (1) subhedral garnets show sharp boundaries with triple junctions among them and against other major mineral constituents (Fig. 3e, f; Supplementary 1b, d), and are evenly distributed, except at intrusive contacts; (2) garnets are homogeneous (Fig. 3e) and free of inclusions and replacement textures, excluding them having a secondary origin (Figs. 3; Supplementary 2); (3) REE and spider diagram patterns of garnets in Wadi El-Hima A-type granites exhibit enrichment of HREE (1531–1742 ppm) relative to LREE (10.2–11.6 ppm), with Eu depletion, similar to profiles documented for magmatic garnets (Fig. 7a, b); (4) our garnets are depleted in Nb and LILE (Ba and Sr) relative to the primitive mantle, suggesting a magmatic origin rather than a hydrothermal origin (Zhou et al. 2017; Sami et al. 2020); (5) the studied garnets crystallized at 680–730 °C and 2.1–2.93 kbar (Supplementary 4) and have similar compositions (Supplementary 6c, 14; Table 2; Supplementary 1) to magmatic garnet in the Strathbogie batholith in Australia (750–850 °C at 1–2 kbar; Phillips et al. 1981) and magmatic almandine-rich garnet (FeO > 30 wt%) that formed from hydrous peraluminous granitic melts (~ 1–3 kbar) in the upper crust (Clemens and Wall 1981). They are also similar to magmatic almandine-rich garnets that crystallized at low pressure (~ 3 kbar) in the southern mountain batholith in Canada (Allan and Clarke 1981). Finally, (6) El-Hima garnets are similar in texture and chemical

compositions to magmatic almandine-rich garnets in Egypt and worldwide (Allan and Clarke 1981; Moghazi et al. 2004; Emam et al. 2011) (Supplementary 6c) and lie in the magmatic field rather than hydrothermal field in common discrimination diagrams (Fig. 14a–f) (Clarke 1981; Miller and Stoddard 1981). As such, we interpret that they crystallized from highly peraluminous granitic magmas.

Factors controlling garnet mineralization and accumulation

The studied I-type garnet-bearing trondhjemites (Figs. 2c, 3a, b) contain less garnet (2–6 vol%) than A-type garnet-rich syenogranites (4–30 vol%) (Figs. 2d–h, 3c–g, Supplementary 1); however, garnet abundance in alkali feldspar granites (1–4 vol%) increases at contacts (up to 8 vol%) or in mixed zones with syenogranites (Fig. 2d). This differs from the reportedly higher concentrations of garnet in I-type granites compared to A-type granites (Chappell and White 1974; Clemens and Wall 1981; Sami et al. 2020). It is, therefore, unclear how the observed high garnet concentration in A-type syenogranites formed, and which factors control garnet mineralization and accumulation in the Wadi El-Hima granites. The studied I-type garnet-bearing trondhjemites have similar garnet contents (2–6 vol%) and compositions (Supplementary 6c) to their protolith tonalites (~ 4–10 vol% garnet; Plimer and Moazzez-Lesco 1980; Moghazi et al. 2004; Thabet 2013); therefore, the composition of the protolith is likely a controlling factor in garnet accumulation in trondhjemites.

Magmatic garnets in the studied syenogranites crystallized directly from highly peraluminous magmas in the upper crust, as discussed above (Fig. 13b). Garnets in both trondhjemites and syenogranites (Fig. 3a–g) have nearly identical compositions (Supplementary 4; Fig. 14) and formed at similar conditions (~ 680–730 °C at 2.1–2.9 kbar), suggesting they share the same peraluminous parent magmas. Garnets in syenogranites reach up to ~ 30 vol% proportion near to and along intrusive contacts with alkali feldspar granites (Figs. 2d–h, 3d–g, 6d; Supplements 1b–d). Hogan (1996) attributed late-stage crystallization of garnets to increasing concentrations of Al in the melt, and we find that this mechanism applies here to the Wadi El-Hima garnet crystallizing from highly peraluminous (A/CNK = 1.04–1.14) magmas as coarse subhedral crystals during late-stage magmatism. Therefore, the appearance of garnet in Wadi El-Hima A-type granites is a result of in situ nucleation from highly peraluminous hydrous magmas (e.g., Clarke 1981; du Bray 1988) (Fig. 13). A contribution to high-volume garnet formation in this case is due to mixing of partially melted tonalitic and metasedimentary protoliths (Fig. 11c–f), which would have been rich in Al and Fe and provided these components to

promote garnet growth and increase its concentrations in syenogranites (Figs. 2d–g, 3d–g).

It is well known that magmatic almandine garnet in peraluminous granites with high silica concentration (~4–10 vol% garnet) generally crystallizes at low pressure conditions (e.g. ~3 kbar; Speer and Becker 1992; Clemens and Wall 1981; Moghazi et al. 2004; Emam et al. 2011; Gharib 2012), which matches the low pressure (up to 3 kbar) and temperature (680–730 °C) conditions recorded by garnets in the Wadi El-Hima granites. Therefore, low pressure and temperature conditions of parent hydrous magmas likely play an important role in crystallization of garnets in Wadi El-Hima granites (Fig. 13). Abundant garnet in the South Eastern Desert granites (e.g. El-Hudi area and Wadi Sikiat) and worldwide (e.g. south mountain batholith in Canada) is related to parental magmas that were mainly peraluminous type (e.g., Emam 2011; Moghazi et al. 2004; Allan and Clarke 1981; Clemens and Wall 1981) and crystallized at low pressure and temperature.

Garnet veins, disseminated and aggregated crystals (Fig. 2d–h) all show concentrations near to and along intrusive contacts (mainly 12–30 vol%; Fig. 6f) with alkali feldspar granites, and decrease in concentration away from this contact (Figs. 3c, 6f). In the study region, NW–SE striking fault zones are considered channels for ascending A-type magmas and juvenile fluids, which enhanced partial melting of garnet-rich syenogranites along the intrusive contact zone. This accumulated residual garnets from the host granites, forming the garnet-rich zone (up to 30 vol% garnet; Figs. 2d–h, 6f, 13) with a NW–SE trend (Fig. 5b) that parallels fault traces of the Najd fault system in the Central Eastern Desert of Egypt. The A-type magmas, which crystallized to form alkali feldspar granites, assimilated syenogranites along the intrusive contact zone (Fig. 2a, b) to form a secondary melt (melt B) and residual garnets (Fig. 13). These garnets were transported long distances within the melts (Dorais and Tubrett 2012) and preferentially accumulated as veins or clots (Figs. 2d–g, 13) by magmatic fluids along intrusive contacts (Creaser et al. 1991) as opposed to areas far away from the contact (Fig. 2d, 6f). This mechanism has been documented via the accumulation of garnets at contact surfaces and shear zones with pegmatites from the Gangdese Orogen in southeastern Tibet (Yu et al. 2021). Therefore, we suggest that the El-Hima garnets in syenogranites and alkali feldspar granites are magmatic origin, but possibly accumulated during a later hydrothermal period. We cannot exclude in situ crystallization of new garnet crystals from melt B, where garnets continued to grow in situ from the melts. Both residual garnets and new garnets with different grain sizes would have been in equilibrium with melt B, and therefore, inherited the same chemical compositions (Supplement 4; Fig. 14). It is well known that garnet may undergo dissolution and reprecipitation, which keeps it in

equilibrium with the changing magma compositions (Dorais and Tubrett 2012).

Based on field investigation, structure lineament extraction mapping (Fig. 5a), and other remote sensing techniques, the Wadi El-Hima area is known to have been affected by the Wadi El-Gemal NW–SE strike-slip fault (Fig. 1c) that lies parallel to the NW–SE Najd fault, and which likely played a role in forming residual garnet accumulations. Moreover, the lineament density map shows a high-density zone near and along contacts of garnet-rich syenogranites with alkali feldspar granites (Fig. 5c). This high-density zone coincides with the existence of faults and fractures, which represent structural pathways for magmatic fluid migration and mineral concentration. Remote sensing spectral mapping via SAM and MF (Fig. 6c, d) indicate that there are very high concentrations of garnets in Wadi El-Hima granites that have the same orientation as NW–SE strike-slip faults (e.g. the Najd fault). Furthermore, the SAM and MF techniques show high distribution of almandine-rich garnets in trondhjemites, syenogranites, alkali feldspar granites and tonalites–granodiorites (G. Umm Asheira) east of the study area, stream sediments, and the pegmatite of Gabal El-Faliq (Fig. 6c, d).

Conclusion

1. Wadi El-Hima I- and A-type mineralized granites in the Eastern Desert of Egypt contain high concentration of magmatic garnets (2–30 vol%), which occur as disseminated subhedral grains, vein-type and aggregated garnet grains. These reflect different mechanisms of accumulation.
2. Applied spectral remote-sensing mapping techniques, such as SAM and MF using VNIR-SWIR ASTER data, indicate high concentrations of garnets in syenogranites and trondhjemites, which are oriented in the NW–SE direction parallel to strike of the Najd fault system. Wadi El-Hima mineralized granites were likely emplaced along a tensional fault zone with a NW–SE strike related to the Najd fault system.
3. El-Hima garnets in trondhjemites are restitic in origin and have been slightly modified by metasomatism. Garnets in syenogranites and alkali feldspar granites are magmatic in origin and crystallized directly from late-stage peraluminous hydrous magmas that were derived from partial melting of tonalitic and metasedimentary protoliths. They are almandine in composition and crystallized at low temperature (~680–730 °C) and pressure (~3 kbar) conditions. They are rich in HREE, Y, Zn, Ga and Li, but are depleted in LILE, Ba, Nb, Sr, Ta, U and Th, with strong negative Eu anomalies, suggesting a magmatic origin.

4. Garnet-bearing trondhjemites have a weakly peraluminous character A/CNK (< 1.1) and low ΣREE (22.4 ppm), and are depleted in Nb, P and Ti, indicating an I-type volcanic arc affinity in an arc-collision setting. In contrast, both garnet-rich syenogranites and alkali feldspar granites have high ΣREE (308.7 ppm) and show strong negative Sr, P, Ti and Eu anomalies, similar to post-collision A-type granites.
5. Both Wadi El-Hima I- and A-type granites crystallized at low pressure (< 3 kbar) in the upper continental crust, but at temperatures of 715 °C and 942 °C, respectively, indicating two stages of magmatism. The old phase of Wadi El-Hima I-type granites (tonalites) formed in a volcanic-arc tectonic setting during collision between a volcanic arc and East Gondwana (~ 650 – 620 Ma), during evolution of the Neoproterozoic juvenile ANS crust. The later phases of A-type granites (~ 630 – 590 Ma) were generated in an orogenic setting during a post-collisional stage.
6. Major factors controlling garnet mineralization in Wadi El-Hima area are: (1) the parent peraluminous hydrous magma composition causing increased in situ nucleation of garnets; (2) deeply sourced magmatic fluids and magmas that migrated upward along NW–SE shear zones to increase anatexis of garnet-bearing syenogranites, forming contact melting zone rich in residual garnets (up to 30 vol%); (3) new garnet crystals may have crystallized in situ from new melts along intrusive contacts; and (4) low pressure (~ 3 kbar) and temperature (~ 680 – 730 °C) conditions are needed to stabilize garnets from hydrous peraluminous magmas.

Supplementary Information The online version contains supplementary material available at <https://doi.org/10.1007/s00531-022-02237-7>.

Acknowledgements The first author is grateful to Missions Sector, Egyptian Ministry of Higher Education for the scholarship and fund to Niigata University 2019–2020 to do mineral and geochemical analyses. The authors are grateful to Prof. Dr. Moustafa Gharib and Dr. Mabrouk Sami for their discussion and comments. We are grateful to Prof. Samir Kamh and the anonymous reviewer for their careful reading of our manuscript and their many insightful comments. We thank Prof. Ulrich Riller (Editor-in-Chief) for his editorial handling of this manuscript.

Funding Open access funding provided by The Science, Technology & Innovation Funding Authority (STDF) in cooperation with The Egyptian Knowledge Bank (EKB).

Open Access This article is licensed under a Creative Commons Attribution 4.0 International License, which permits use, sharing, adaptation, distribution and reproduction in any medium or format, as long as you give appropriate credit to the original author(s) and the source, provide a link to the Creative Commons licence, and indicate if changes were made. The images or other third party material in this article are included in the article's Creative Commons licence, unless indicated otherwise in a credit line to the material. If material is not included in

the article's Creative Commons licence and your intended use is not permitted by statutory regulation or exceeds the permitted use, you will need to obtain permission directly from the copyright holder. To view a copy of this licence, visit <http://creativecommons.org/licenses/by/4.0/>.

References


- Abdel-Rahman AFM (1994) Nature of biotites from alkaline, calc-alkaline, and peraluminous magmas. *J Petrol* 35:525–541
- Aboelkhair H, Ninomiya Y, Watanabe Y, Sato I (2010) Processing and interpretation of ASTER TIR data for mapping of rare-metal-enriched albite granitoids in the Central Eastern Desert of Egypt. *J Afr Earth Sci* 58:141–151
- Abrams M (2000) The Advanced Spaceborne Thermal Emission and Reflection Radiometer (ASTER): data products for the high spatial resolution imager on NASA's Terra platform. *Int J Remote Sens* 21:847–859
- Akinin VV, Miller EL, Wooden JL (2009) Petrology and geochronology of crustal xenoliths from the Bering Strait region: linking deep and shallow processes in extending continental crust. Crustal cross sections from the western North American Cordillera and elsewhere: implications for tectonic and petrologic processes. *Geol Soc Am Spec Paper* 456:39–68
- Allan BD, Clarke DB (1981) Occurrence and origin of garnets in the South Mountain batholith, Nova Scotia. *Can Mineral* 19:19–24
- Amer R, Kusky T, Ghulam A (2010) Lithological mapping in the Central Eastern Desert of Egypt using ASTER data. *J Afr Earth Sci* 56:75–82
- Asran AM, Emam A, El-Fakharani A (2017) Geology, structure, geochemistry and ASTER-based mapping of Neoproterozoic Gebel El-Delhimmi granites, Central Eastern Desert of Egypt. *Lithos* 282:358–372
- Avigad D, Gvirtzman Z (2009) Late Neoproterozoic rise and fall of the northern Arabian Nubian Shield: the role of lithospheric mantle delamination and subsequent thermal subsidence. *Tectonophysics* 477:217–228
- Azer MK, Abdelfadil KM, Ramadan AA (2019) Geochemistry and petrogenesis of Late Ediacaran Rare-Metal Albite Granite of the Nubian Shield: case study of Nuweibi Intrusion, Eastern Desert, Egypt. *J Geol* 127:665–689
- Barker F (1979) Trondhjemite: Definition, environment and hypotheses of origin. In trondhjemites, dacites, and related rocks. *Dev Petrol* 6:1–12
- Barker F, Arth JG (1976) Generation of trondhjemitic-tonalitic liquids and Archean bimodal trondhjemite-basalt suites. *Geology* 4:596–600
- Bhattacharya A, Mohanty L, Maji A, Sen SK, Raith M (1992) Non-ideal mixing in the phlogopite-annite binary: constraints from experimental data on Mg–Fe partitioning and a reformulation of the biotite-garnet geothermometer. *Contrib Mineral Petrol* 111:87–93
- Chappell BW, White AJR (1974) Two contrasting granite types. *Pac Geol* 8:173–174
- Chappell BW, White AJR (1992) I- and S-type granites in the Lachlan Fold Belt. *Earth Environ Sci Trans R Soc Edinb* 83:1–26
- Chavez PS, Berlin GL, Sowers LB (1982) Statistical method for selecting landsat MSS. *J Appl Photogr Eng* 8:23–30
- Clarke DB (1981) The mineralogy of peraluminous granites; a review. *Can Mineral* 19:3–17
- Clarke DB, Rottura A (1994) Garnet-forming and garnet-eliminating reactions in a quartz diorite intrusion at Capo Vaticano, Calabria, Italy. *Can Mineral* 32:623–635

- Clemens JD, Wall VJ (1981) Origin and crystallization of some peraluminous (S-type) granitic magmas. *Can Mineral* 19:111–131
- Creaser RA, Price RC, Wormald RJ (1991) A-type granites revisited: assessment of a residual-source model. *Geology* 19:63–166
- Dahlquist JA, Galindo C, Pankhurst RJ, Rapela CW, Alasino PH, Saavedra J, Fanning CM (2007) Magmatic evolution of the Peñón Rosado granite: petrogenesis of garnet-bearing granitoids. *Lithos* 95:177–207
- De la Roche H, Leterrier J, Grandclaude MM (1980) A classification of volcanic and plutonic rocks using R1–R2 diagram and major element analyses-its relationships with current nomenclature. *Chem Geol* 29:183–210
- De Paolo DJ (1981) Trace element and isotopic effects of combined wall rock assimilation and fractional crystallization. *Earth Planet Sci Lett* 53:189–202
- Deer WA, Howie RA, Zussman J (1992) An Introduction to the rock forming minerals, 2nd Longman edn. Longman, London
- Dorais M, Campbell S (2022) Peritectic and phenocrystic garnet accumulation and the origin of strongly peraluminous granitic rocks: the Flagstaff Lake Igneous Complex, Maine. *Lithos* 418–419:106680
- Dorais MJ, Tubrett M (2012) Detecting peritectic garnet in the peraluminous Cardigan Pluton, New Hampshire. *J Petrol* 53:299–324
- Drummond MS, Ragland PC, Wesolowski D (1986) An example of trondhjemite genesis by means of alkali metasomatism: rock-ford granite, Alabama Appalachians. *Contrib Mineral Petrol* 93:98–113
- Drury S (1993) Image interpretation in geology, 2nd edn. Chapman and Hall, London, p 283
- du Bray EA (1988) Garnet compositions and their use as indicators of peraluminous granitoid petrogenesis-southeastern Arabian Shield. *Contrib Mineral Petrol* 100:205–212
- Eby GN (1992) Chemical subdivision of the A-type granitoids: petrogenetic and tectonic implications. *Geology* 20:641–644
- El-Bialy MZ, Omar MM (2015) Spatial association of Neoproterozoic continental arc I-type and post-collision A-type granitoids in the Arabian-Nubian Shield: the Wadi Al-Baroud Older and Younger Granites, North Eastern Desert, Egypt. *J Afr Earth Sci* 103:1–29
- Eliwa HA, Breitreuz C, Murata M, Khalaf IM, Bühler B, Itaya T, Takahashi T, Hirahara Y, Miyazaki T, Kimura JI, Shibata T (2014) SIMS zircon U–Pb and mica K–Ar geochronology, and Sr–Nd isotope geochemistry of neoproterozoic granitoids and their bearing on the evolution of the north Eastern Desert, Egypt. *Gondw Res* 25:1570–1598
- Emam A, Moghazy NM, El-Sherif AM (2011) Geochemistry, petrogenesis and radioactivity of El Hudi I-type younger granites, South Eastern Desert, Egypt. *Arab J Geosci* 4:863–878
- Erdmann S, Jamieson RA, MacDonald MA (2009) Evaluating the origin of garnet, cordierite, and biotite in granitic rocks: a case study from the South Mountain Batholith, Nova Scotia. *J Petrol* 50:1477–1503
- Eyal M, Litvinovsky B, Jahn BM, Zanzivlevich A, Katzir Y (2010) Origin and evolution of post-collisional magmatism: Coeval Neoproterozoic calc-alkaline and alkaline suites of the Sinai Peninsula. *Chem Geol* 269:153–179
- Farahat ES, Mohamed HA, Ahmed AF, El Mahallawi MM (2007) Origin of I- and A-type granitoids from the eastern desert of Egypt: Implications for crustal growth in the northern Arabian-Nubian Shield. *J Afr Earth Sci* 49:43–58
- Frost BR, Barnes CG, Collins WJ, Arculus RJ, Ellis DJ, Frost CD (2001) A geochemical classification for granitic rocks. *J Petrol* 42:2033–2048
- Gaspar M, Knaack C, Meinert LD, Moretti R (2008) REE in skarn systems: a LA-ICP-MS study of garnets from the Crown Jewel gold deposit. *Geochim Cosmochim Acta* 72:185–205
- Gerdes A, Worner G, Henk A (2000) Post-collisional granite generation and HT–LP metamorphism by radiogenic heating: the Variscan South Bohemian Batholith. *J Geol Soc* 157:577–587
- Gharib ME (2012) Origin and evolution history of magmatic garnet-bearing pegmatites and associated granitoids, Abu Had area, South Eastern Desert, Egypt: inference from petrology and geochemistry. *J Am Sci* 8:536–554
- Green TH (1977) Garnet in silicic liquids and its possible use as a P–T indicator. *Contrib Mineral Petrol* 65:59–67
- Green TH (1995) Significance of Nb/Ta as an indicator of geochemical processes in the crust-mantle system. *Chem Geol* 120:347–359
- Green TH, Ringwood AE (1968) Origin of garnet phenocrysts in calc-alkaline rocks. *Contrib Mineral Petrol* 18:163–174
- Gromet LP, Silver LT (1983) Rare earth element distributions among minerals in a granodiorite and their petrogenetic implications. *Geochim Cosmochim Acta* 47:925–939
- Harangi Z, Downes H, Kósa L, Szabó CS, Thirlwall MF, Mason PRD, Matthey D (2001) Almandine garnet in calc-alkaline volcanic rocks of the Northern Pannonian Basin (Eastern–Central Europe): geochemistry, petrogenesis and geodynamic implications. *J Petrol* 42:1813–1843
- Hassan MA, Hashad AH (1990) Precambrian of Egypt. In: Said R (ed) *The geology of Egypt*. Balkema, Rotterdam, pp 201–245
- Heikal MTS, Khedr MZ, El-Monesf MA, Gomaa SR (2019) Petrogenesis and geodynamic evolution of Neoproterozoic Abu Dabbab Albite Granite, Central Eastern Desert of Egypt: petrological and geochemical constraints. *J Afr Earth Sci* 158:103518
- Helmy HM, Ahmed AF, El Mahallawi MM, Ali SM (2004) Pressure, temperature and oxygen fugacity conditions of calc-alkaline granitoids, Eastern Desert of Egypt, and tectonic implications. *J Afr Earth Sci* 38:255–268
- Hey MH (1954) A new review of chlorites. *Mineral Mag* 30:278–292
- Hogan JP (1996) Insight from igneous reaction space: a holistic approach to granite crystallization. *Trans R Soc Edinb Earth Sci* 87:147–157
- Holdaway MJ (2000) Application of new experimental and garnet Margules data to the garnet-biotite geothermometer. *Am Mineral* 85:881–892
- Holtz F, Behrens H, Dingwell DB, Taylor RP (1992) Water solubility in aluminosilicate melts of haplogranite composition at 2 kbar. *Chem Geol* 96:289–302
- Hung L, Batelaan O, De Smedt F (2005) Lineament extraction and analysis, comparison of LANDSAT ETM and ASTER imagery. Case study: Suoimuoi tropical karst catchment, Vietnam. *Remote Sens Environ Monit GIS Appl Geol* 5983:59830–59832
- Ismail T (2013) Petrological and microstructural evolution of syntectonic granitoids rocks, Migif-Hafait area, South Eastern desert, Egypt (No. GRI-2013-11015). Aristotle University of Thessaloniki
- Izawa MRM, Cloutis EA, Rhind T, Mertzman SA, Poitras J, Applin DM, Mann P (2018) Spectral reflectance (0.35–2.5 μm) properties of garnets: implications for remote sensing detection and characterization. *Icarus* 300:392–410
- Johnson PR, Andresen A, Collins AS, Fowler AR, Fritz H, Ghebreab W, Kusky T, Stern RJ (2011) Late Cryogenian–Ediacaran history of the Arabian-Nubian Shield: a review of depositional, plutonic, structural, and tectonic events in the closing stages of the northern East African Orogen. *J Afr Earth Sci* 61:167–232
- Kontak DJ, Corey M (1988) Metasomatic origin of Spessartine-rich garnet in the South Mountain Batholith, Nova-Scotia. *Can Mineral* 26:315–334
- Kröner A, Krüger J, Rashwan AAA (1994) Age and tectonic setting of granitoid gneisses in the Eastern Desert of Egypt and south-west Sinai. *Geol Rundsch* 83:502–513

- Kruse FA, Lefkoff AB, Boardman JW, Heidebrecht KB, Shapiro AT, Barloon PJ, Goetz AFH (1993) The spectral image processing system (SIPS)-interactive visualization and analysis of imaging spectrometer data. *Remote Sens Environ* 44:145–163
- Laurent O, Martin H, Moyen JF, Doucelance R (2014) The diversity and evolution of late-Archean granitoids: evidence for the onset of “modern-style” plate tectonics between 3.0 and 2.5 Ga. *Lithos* 205:208–235
- Leake BE, Woolley AR, Arps CE, Birch WD, Gilbert MC, Grice JD, Hawthorne FC, Kato A, Kisch HJ, Krivovichev VG, Linthout K (1997) Nomenclature of amphiboles; report of the subcommittee on amphiboles of the International Mineralogical Association, Commission on New Minerals and Mineral Names. *Can Mineral* 35:219–246
- Li ZH, Liu M, Gerya T (2016) Lithosphere delamination in continental collisional orogens: a systematic numerical study. *J Geophys Res Solid Earth* 121:5186–5211
- Madani A, Emam A (2011) SWIR ASTER band ratios for lithological mapping and mineral exploration: a case study from El Hudi area, southeastern desert, Egypt. *Arab J Geosci* 4:45–52
- Maniar PD, Piccoli PM (1989) Tectonic discrimination of granitoids. *Geol Soc Am Bull* 101:635–643
- Manning DAC (1981) The effect of fluorine on liquidus phase relationships in the system $Qz-Ab-Or$ with excess water at 1 kb. *Contrib Mineral Petrol* 76:206–215
- Meyer SE, Passchier C, Abu-Alam T, Stüwe K (2014) A strike-slip core complex from the Najd fault system, Arabian shield. *Terra Nova* 26:387–394
- Miller CF, Stoddard EF (1981) The role of manganese in the paragenesis of magmatic garnet: an example from the old woman-Piute Range, California: a reply. *J Geol* 89:770–772
- Miller C, Thoni M, Frank W, Grasemann B, Klotzli U, Guntli P, Draganits E (2001) The early Palaeozoic magmatic event in the Northwest Himalaya, India: source, tectonic setting and age of emplacement. *Geol Mag* 138:237–251
- Moghazi AM, Hassanen MA, Mohamed FH, Ali S (2004) Late Neoproterozoic strongly peraluminous syenogranites, South Eastern Desert, Egypt—petrogenesis and geodynamic significance. *Mineral Petrol* 81:19–41
- Nachit H, Ibhi A, Abia EH, Ohoud MB (2005) Discrimination between primary magmatic biotites, reequilibrated biotites and neoformed biotites. *Comptes Rendus Géoscience* 337:1415–1420
- Nicolae I, Saccani E (2003) Petrology and geochemistry of the Late Jurassic calc-alkaline series associated to Middle Jurassic ophiolites in the South Apuseni Mountains (Romania). *Swiss Bull Mineral Petrol* 83:81–96
- Palin RM, White RW, Green EC, Diener JF, Powell R, Holland TJ (2016) High-grade metamorphism and partial melting of basic and intermediate rocks. *J Metamorph Geol* 34:871–892
- Patino Douce AE (1999) What do experiments tell us about the relative contributions of crust and mantle to the origin of granitic magmas. *Geol Soc Lond Spec Publ* 168:55–75
- Pearce JA, Harris NBW, Tindle AG (1984) Trace element discrimination diagrams for the tectonic interpretation of granitic rocks. *J Petrol* 25:956–983
- Pearce NJG, Perkins WT, Westgate JA, Gorton MP, Jackson SE, Neal CR, Chenery SP (1997) A compilation of new and published major and trace element data for NIST SRM 610 and NIST SRM 612 glass reference materials. *Geostand Newslett* 21:115–144
- Phillips GN, Wall VJ, Clemens JD (1981) Petrology of the Strathbogie Batholith; a cordierite-bearing granite. *Can Mineral* 19:47–63
- Plimer IR, Moazzez-Lesco Z (1980) Garnet xenocrysts in the Mashhad granite, NE Iran. *Geol Rundsch* 69:801–810
- Pour AB, Hashim M (2012) Identifying areas of high economic-potential copper mineralization using ASTER data in the Urumieh-Dokhtar Volcanic Belt, Iran. *Adv Space Res* 49:753–769
- Pownceby MI, Wall VJ, O'Neill HSIC (1987) Fe–Mn partitioning between garnet and ilmenite: experimental calibration and applications. *Contrib Mineral Petrol* 97:116–126
- Pownceby MI, Wall VJ, O'Neill HSC (1991) An experimental study of the effect of Ca upon garnet-ilmenite Fe–Mn exchange equilibria. *Am Mineral* 76:1580–1588
- Qin Q, Wang T, Huang H, Zhang Z, Tong Y, Song P, Zhang J (2021) Late Carboniferous and Early Permian garnet-bearing granites in the South Tianshan Belt, NW China: Two Late Paleozoic magmatic events and implications for crustal reworking. *J Asian Earth Sci* 220:104923
- Rene M, Stelling J (2007) Garnet-bearing granite from the Třebíč pluton, Bohemian massif (Czech Republic). *Mineral Petrol* 91:55–69
- Richards JA, Xiuping J (2006) Remote sensing digital image analysis: an introduction, vol 3. Springer, Berlin, pp 10–38
- Robinson FA, Bonin B, Pease V, Anderson JL (2017) A discussion on the tectonic implications of Ediacaran late-to post-orogenic A-type granite in the northeastern Arabian Shield, Saudi Arabia. *Tectonics* 36:582–600
- Rudnick RL, Fountain DM (1995) Nature and composition of the continental crust: a lower crustal perspective. *Rev Geophys* 33:267–309
- Sadek M, Ali-Bik MW, Hassan SM (2015) Late Neoproterozoic basement rocks of Kadabora-Suwayqat area, Central Eastern Desert, Egypt: geochemical and remote sensing characterization. *Arab J Geosci* 8:10459–10479
- Saleh GM, Salem IA, Darwish ME, Mostafa DA (2014) Gabal El Faliq granitoid rocks of the southeastern Desert, Egypt: geochemical constraints, mineralization and spectrometric prospecting. *World J Earth Planet Sci* 1:1–12
- Samadi R, Miller NR, Mirnejad H, Harris C, Kawabata H, Shirdashtzadeh N (2014) Origin of garnet in aplite and pegmatite from Khajeh Morad in northeastern Iran: a major, trace element, and oxygen isotope approach. *Lithos* 208:378–392
- Samadi R, Torabi G, Kawabata H, Miller NR (2021) Biotite as a petrogenetic discriminator: chemical insights from igneous, meta-igneous and meta-sedimentary rocks in Iran. *Lithos* 386:106016
- Sami M, Ntaflou T, Farahat ES, Mohamed HA, Ahmed AF, Hauzenberger C (2017) Mineralogical, geochemical and Sr–Nd isotopes characteristics of fluorite-bearing granites in the Northern Arabian-Nubian Shield, Egypt: constraints on petrogenesis and evolution of their associated rare metal mineralization. *Ore Geol Rev* 88:1–22
- Sami M, Ntaflou T, Mohamed HA, Farahat ES, Hauzenberger C, Mahdy NM, Abdelfadil KM, Fathy D (2020) Origin and petrogenetic implications of spessartine garnet in highly-fractionated granite from the Central Eastern Desert of Egypt. *Acta Geologica Sinica Engl Ed* 94:763–776
- Schott B, Schmeling H (1998) Delamination and detachment of a lithospheric root. *Tectonophysics* 296:225–247
- Seddik AM, Darwish MH, Azer MK, Asimow PD (2020) Assessment of magmatic versus post-magmatic processes in the Mueilha rare-metal granite, Eastern Desert of Egypt, Arabian-Nubian Shield. *Lithos* 366:105542
- Shawky MM, El-Arafy RA, El Zalaky MA, Elarif T (2019) Integrated image processing and GIS-based techniques using knowledge-driven approaches to produce potential radioactivity map for the uraniferous granite of Egypt. *NRIAG J Astron Geophys* 8:185–197
- Speer JA, Becker SW (1992) Evolution of magmatic and subsolidus AFM mineral assemblages in granitoid rocks: biotite, muscovite, and garnet in the Cuffytown Creek, pluton, South Carolina. *Am Mineral* 77:821–833

- Stern RJ (1994) Arc-assembly and continental collision in the Neoproterozoic African orogen: implications for the consolidation of Gondwanaland. *Annu Rev Earth Planet Sci* 22:319–351
- Stern RJ (2002) Crustal evolution in the East African Orogen: a neodymium isotopic perspective. *J Afr Earth Sci* 34:109–117
- Stern RJ, Hedge CE (1985) Geochronologic and isotopic constraints on late Precambrian crustal evolution in the Eastern Desert of Egypt. *Am J Sci* 285:97–127
- Sultan M, Arvidson RE, Duncan IJ, Stern RJ, El Kaliouby B (1988) Extension of the Najd shear system from Saudi Arabia to the central Eastern Desert of Egypt based on integrated field and Landsat observations. *Tectonics* 7:1291–1306
- Sun SS, McDonough WF (1989) Chemical and isotopic systematics of oceanic basalts: implications for mantle composition and processes. *Geol Soc Lond Spec Publ* 42:313–345
- Taylor SR, McLennan SM (1985) The continental crust: its composition and evolution. Blackwell, Oxford, p 312
- Taylor J, Stevens G (2010) Selective entrainment of peritectic garnet into S-type granitic magmas: evidence from Archaean mid-crustal anatectites. *Lithos* 120:277–292
- Thabet I (2013) Petrological and microstructural evolution of syn-tectonic granitoids rocks, Magic-Haffit area, South Eastern desert, Egypt (No. GRI-2013-11015). PhD Thesis, Aristotle University of Thessaloniki, p 203
- Vincent RK (1997) Fundamentals of geological and environmental remote sensing. Prentice Hall 1st edition, Upper Saddle River, p 370.
- Watson EB, Harrison TM (1983) Zircon saturation revisited: temperature and composition effects in a variety of crustal magma types. *Earth Planet Sci Lett* 64:295–304
- Whalen JB, Currie KL, Chappell BW (1987) A-type granites: geochemical characteristics, discrimination and petrogenesis. *Contrib Mineral Petrol* 95:407–419
- Wones DR (1989) Significance of the assemblage titanite + magnetite + quartz in granitic-rocks. *Am Mineral* 74:744–749
- Wu CM (2019) Original calibration of a garnet geobarometer in metapelite. *Minerals* 9:540. <https://doi.org/10.3390/min9090540>
- Yang XM (2017) Estimation of crystallization pressure of granite intrusions. *Lithos* 286:324–329
- Yu M, Xia QX, Zheng YF, Zhao ZF, Chen YX, Chen RX, Luo X, Li WC, Xu H (2021) The composition of garnet in granite and pegmatite from the Gangdese orogen in southeastern Tibet: constraints on pegmatite petrogenesis. *Am Mineral* 106:265–281
- Zhang Y, Shao YJ, Wu CD, Chen HY (2017) LA-ICP-MS trace element geochemistry of garnets: Constraints on hydrothermal fluid evolution and genesis of the Xinqiao Cu–S–Fe–Au deposit, eastern China. *Ore Geol Rev* 86:426–439
- Zhou J, Feng C, Li D (2017) Geochemistry of the garnets in the Baiguanhu W–Sn ore field, NW China. *Ore Geol Rev* 82:70–92

Authors and Affiliations

Mohamed Zaki Khedr¹  · Saif M. Abo Khashaba¹ · N. H. El-Shibiny¹ · Reda A. El-Arafy² · Eiichi Takazawa³ · Mokhles K. Azer⁴ · Richard. M. Palin⁵

¹ Geology Department, Faculty of Science, Kafrelsheikh University, Kafrelsheikh 33516, Egypt

² Remote Sensing and GIS Department, Nuclear Materials Authority, Cairo, Egypt

³ Geology Department, Faculty of Science, Niigata University, Niigata 950-2181, Japan

⁴ Geological Sciences Department, National Research Centre, Cairo, Egypt

⁵ Department of Earth Sciences, University of Oxford, Oxford OX1 3AN, UK